Department of Physics and Astronomy
University of Heidelberg

Diploma thesis
in Physics

submitted by
Katharina Alexandra Otto
born in Geseke

2011

Calibration of the Position Sensitive Beam Monitor of the Heidelberg Dust Accelerator

This diploma thesis has been carried out by

Katharina Alexandra Otto

at the

Max Planck Institute for Nuclear Physics in Heidelberg

under the supervision of

Prof. Dr. Eberhard Grün

Kalibration des Positionsdetektors am Heidelberger Staubbeschleuniger:

Um die Trajektorie eines Staubteilchens zu bestimmen, wurde ein neu entwickelter Positionsdetektor im Strahlrohr des Heidelberger Staubbeschleunigers eingebaut. Dieser ermöglicht es, die Position eines Staubteilchens zu ermitteln ohne die Bewegung des Teilchens dabei zu beeinflussen, indem das Prinzip der elektrischen Induktion ausgenutzt wird.
Diese Arbeit beschreibt die Kalibrationsmethode und ihre Ergebnisse, die nun benutzt werden können, um ein Detektorsignal einer Position im Strahlrohr zuzuordnen. Zusätzlich wurde eine idealisierte Simulation erstellt, um die experimentellen Ergebnisse zu unterstützen. Die Genauigkeit des Detektors für verschiedene Signal zu Rausch Verhältnisse (SNR) und die Ladungsdetektionsgrenze wurden ermittelt und stellen den Positionsdetektor als wertvolle und verlässliche Ergänzung des Staubbeschleunigers dar.
Als eine zweite unabhängige Positionsmessung wurde ein segmentiertes Target in das Strahlrohr eingebaut, um einen Staubeinschlag mit einem Detektorsignal zu korrelieren. Die resultierende Kalibrationskurve erlaubt es die Detektorgenauigkeit mit 0.3 mm bei einem SNR von 20 dB anzuschätzen. Die Ladungsgrenze des Detektors wurde durch die Auswertung des Rauschens zu 1.23 fC für Teilchen im Zentrum des Strahlrohrs bestimmt.
Die Detektorsimulation, die mit dem Softwareprogramm Coulomb berechnet wurde, wurde benutzt um eine Kalibrationskurve zu erstellen, die die experimentellen Ergebnisse unterstützend widerspiegelt.

Calibration of the Position Sensitive Beam Monitor of the Heidelberg Dust Accelerator:

To ascertain a dust particle's trajectory a new developed position sensitive detector was implemented in the beam line of the Heidelberg Dust Accelerator. It allows to determine a dust particle's position without effecting its movement by using the principle of electric induction.
This work describes the calibration method and its results that now can be used to map a detector signal to a particle position in the beam line. Additionally an idealised simulation was used to calculate the expected signals. The accuracy of the detector for various signal to noise ratios (SNR) and the charge detection limit was determined.
As a secondary independent position measurement a segmented impact target was installed in the beam line to correlate a dust impact and a detector signal. The resulting calibration curve yielded to an estimate of the detector accuracy of about 0.3 mm based on a SNR of 20 dB. By evaluating the noise of the detector, the charge detection limit was determined to be 1.23 fC for particles passing through the center of the beam line.
The detector simulation, calculated with the software programme Coulomb, was used to produce a calibration curve that represents the experimental results supportingly.

Contents

1 Introduction

When thinking about space, one thing that surely comes in to one's mind is its infinite dimension. Everything seems to be far away and much larger than we can imagine living on Earth; the stars and their planets, the Milky Way or galaxies are found millions of light years away from where we take our observations. But we do not have to think in such large dimensions to investigate these objects. In fact there is a component in space that is able to help us understand many things about them that is so tiny that we cannot even see it with the naked eye. This is cosmic dust.

The space between planets and stars is not empty but filled with gas and dust. They are present at the formation of new stars and are the source of their planets but they are also the product after a star's decay. As cosmic dust accompanies the evolution of stars and formation of planetary systems, we can understand these processes better by exploring the dust.

The dust grains are tiny particles ranging in size from a few nanometres up to grains which are large enough (some hundreds of micrometres) for their motion to be dominated by gravity [Grün et al., 1994]. There are three different "families" of dust: planetary, interplanetary and interstellar dust.

Planetary dust describes particles that are bound to and originate from a planet or moon in the solar system. A well-known example are Saturn's dust rings currently investigated by the Cassini spacecraft's Cosmic Dust Analyzer (CDA). As an example Saturn's E-ring is fed by its moon Enceladus' dust plumes and so has a "planetary" origin while remaining bound to Saturn by its gravity [Porco et al., 2006]. The dust particles' typical speeds when bound to a planetary system are about a few km/s. But due to planetary electromagnetic fields they can be accelerated up to 300 km/s. Dust grains in space are charged by photoelectronic emission by UV radiation and by interaction with the ambient plasma. These dust particles can then be forced onto trajectories that move them out of the planetary or even solar system. This was finally observed in the Jovial system by Grün and Landgraf [2001].

Interplanetary dust particles are grains that are located and originated in the

solar system but are not bound to a planet. They cause the effect of zodiacal light observable on Earth by scattering sunlight in the ecliptic [Grün et al., 2001, ch. 1.2]. These particles have different origins such as asteroid collisions or outgassing comets. Interplanetary dust from comet Wild 2 was collected in aerogel cubes by the Stardust sample return mission and successfully brought to Earth for further investigation in 2006 [Flynn et al., 2006; Brownlee et al., 2006].

The term interstellar dust is used for dust particles that originate from old giant stars and possible supernova and novae explosions and that fill the space between the stars [Amari and Lodders, 2006]. It was first detected by the extinction and polarization of starlight. These dust particles also enter the solar system and can be distinguished from interplanetary dust by their trajectories through the solar system. Their first detection was by the Ulysses spacecraft in 1993 [Grün et al., 1993].

There are different ways to investigate cosmic dust. Observation of the spectra and scattering of zodiacal light gives information about the grains' sizes and chemical compositions. This observation is completed by in situ measurements of cosmic dust such as CDA charge and composition data and sample return missions like the Stardust mission.

A challenge in investigating cosmic dust is that the observations have to be carried out in space. Even though tonnes of cosmic dust impacts the Earth daily it is nearly impossible to distinguish the tiny dust grains from terrestrial grains once they reach the atmosphere. A major task before sending a new dust instrument to explore space is calibrating and testing it. For this reason the Heidelberg Dust Accelerator was built at the Max Planck Institute for Nuclear Physics in Heidelberg. A 2 MV Van de Graaff generator accelerates charged dust particles to speeds similar to those found in space, depending on their size and mass. Space in situ instruments like the CDA were calibrated in the dust accelerator's beam line. Also impact studies and plasma physics are investigated with the help of the dust accelerator.

When dust impact studies, such as the investigation of impact tracks in aerogel or crater studies on foils, are made with the help of the dust accelerator it is

especially interesting to determine the dust particles' locations precisely. This is useful in reducing the effort of finding the mostly micrometre-sized impact features on a target that is thousands of times larger. Particle properties may then be mapped to an impact track or crater on a target. Recently a new position sensitive detector was designed and added to the dust accelerator's beam line for this purpose.

1.1 About this Thesis

This thesis describes the functionality and calibration of the position sensitive detector. It explains the general principles of the detector and describes ways of calibrating and evaluating its signals.
The detector works by detecting the induced charge of a dust particle on four plates connected to a single charge amplifier and thus producing one signal corresponding to the particle position. A method of how to map a signal from the position sensitive detector to a particle position in the beam line is determined by locating the impact location of the dust particle, after passing through the detector, using a second independent measurement. For this reason an impact target with separate segments was installed behind the position detector. The segments were attached to different charge amplifiers that allowing an impact on a segment to be detected. This yielded a calibration curve that maps the particle location to a position detector signal.
The charge sensitivity and accuracy of the detector are also discussed. For this reason the average noise and disturbances on the detector were determined and their influence on the signal and thus spatial precision was analysed depending on the signal to noise ratio (SNR).
In addition to the measurement, a simulation of the detector signals was generated to support the experimental results. With the help of the programme Coulomb [2011] the signals for various particle trajectories were calculated and compared to the measured signals. Thus the deviation of the detector signals from the ideal simulated signals, caused for example by detector shielding, could

be analysed and discussed.
In Chapter 2 of this thesis the functionality of the dust accelerator and its dust source and focusing are explained. Later a description of the position sensitive detector is given. The physical principles behind the process of induction and how this concept was used to determine a charge's location in between two conductive plates are explained with respect to the set up of the position sensitive detector. The functionality of a charge amplifier as employed in the detector set up is characterised and a short overview of earlier position detectors is presented. Additionally the calibration principle and assembly is demonstrated.
Chapter 3 outlines the measurement and the simulation of the detector performance calculated for the detector signals with Coulomb [2011].
This is followed by the results chapter. Firstly an overview of recorded detector signals is given. The data evaluation leading to a calibration curve of the position detector as derived from the experiment and the simulation follows. Also the accuracy and charge sensitivity of the detector is determined. This is supplemented by the simulation results and the simulated calibration curve. The effect of charge loss, for example caused by the detector's shielding is also discussed as derived from the simulation results.
A discussion and a summary is given in Chapter 5. It compares the results produced by the experiment with those derived from the simulation and summarizes the important facts of the position sensitive detector from the results section.
The outlook suggests improvements to the detector assembly. The effect of reducing the plate distance and how this may improve the detector accuracy is discussed. It also introduces the idea of an additional calibration set up which detects the light flash produced by a dust impact with a light amplifier. The evaluation software's instructions are given in the appendix.

2 Experimental Setup

2.1 Dust Accelerator Assembly

2.1.1 Dust Accelerator

In order to investigate dust impacts on various targets and calibrate space dust instruments the Max Planck Institute for Nuclear Physics in Heidelberg operates a 2 MV Van de Graaff dust accelerator. The generator works by separating electric charges with a circulating belt. Negative charges are stripped from the belt, hence, positive charges are transported to the "terminal" of the accelerator where they induce a positive potential with respect to ground.
A smooth potential gradient between the terminal and earth is maintained by 60 equipotential rings connected by 1.2 GΩ resistors. The dust source which produces positively charged dust particles is located inside the terminal under vacuum. Thus the positively charged dust grains are accelerated through the potential after leaving the dust source and continue through the beam line, which is held at a vacuum of about 10^{-6} mbar, to the experiments as shown in Fig. 2.1. The terminal is surrounded by a pressure tank filled with SF_6 gas at pressures of up to 16 bar to help prevent flash-overs.
After being accelerated the dust particles pass several detectors, which form the Particle Selection Unit (PSU). The PSU determines their speeds and charges by induction. The selected particles pass the PSU while the unsuitable dust grains are deflected by plate capacitors.
By knowing a dust particle's speed v and charge q the mass m can be determined by equating their kinetic and electrical potential energy:

$$\frac{1}{2}mv^2 = qU_{pot} \tag{2.1}$$

Here U_{pot} is the accelerating potential. Thus the mass m of the particle is:

$$m = \frac{2qU_{pot}}{v^2} \tag{2.2}$$

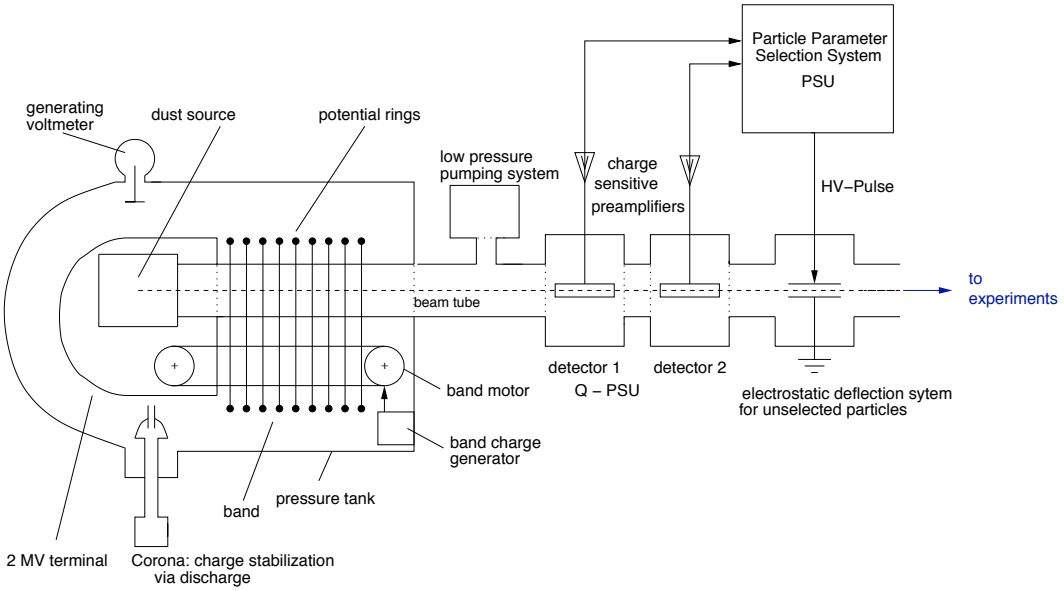

Figure 2.1: Schematic of the Heidelberg Dust Accelerator (after Fig. 3.10 in Mocker [2011]).

To determine the relationship between a particle's size and speed, the fact that a particle is able to carry more charge on a larger surface area has to be taken in account. Assuming a homogeneous sphere and density for a particle the relationship between mass m and radius r is given by

$$m \propto r^3 \tag{2.3}$$

because the mass is proportional to the volume when homogeneous density is assumed. For a constant surface field strength on a charged dust particle the relationship between charge q and particle radius r is given by

$$q \propto r^2 \tag{2.4}$$

as the surface area increases in proportion to the square of a sphere's radius. Introducing this into Eq. 2.1 gives:

$$r^3 v^2 \propto r^2 U_{pot} \tag{2.5}$$

and thus

$$r \propto v^{-2} \tag{2.6}$$

$$m \propto v^{-6} \tag{2.7}$$

$$q \propto v^{-4}. \tag{2.8}$$

So the charge to mass ratio is given by

$$\frac{q}{m} \propto \frac{1}{r} \propto v^2 \tag{2.9}$$

Thus the smallest particles have the highest charge to mass ratio and so are the fastest [Fechtig et al., 1978, ch. 9].

2.1.2 Dust Source and Particles

At the terminal of the dust accelerator an exchangeable dust source is attached to supply the accelerator with charged particles.
The dust source is placed at a potential of 2 MV. Inside the source, in a cylindrical reservoir of 10 mm diameter and 25 mm length, the dust particles are dispersed by a positive 20 kV alternating voltage delivered by the reservoir housing. The needle is sharpened to a few micrometres at the tip and placed in the axis of the source's dust reservoir as seen in Fig. 2.2 [Stübig et al., 2001]. It functions as a charging electrode with a positive potential.
The field strength at the tip of the tungsten needle is given by:

$$E = \frac{U_{needle}}{d} \tag{2.10}$$

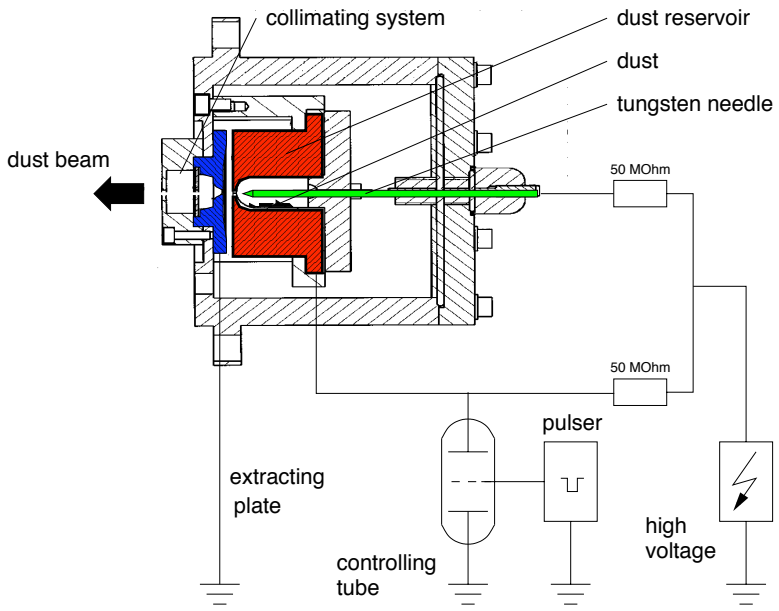

Figure 2.2: Schematic of the dust source inside the Heidelberg Dust Accelerator (after Fig. 3.12 in Mocker [2011]).

where d is the diameter of the needle tip and U the potential of the needle with respect to the reservoir. Assuming a tip diameter of 5 μm and a reservoir potential of 20 kV this leads to:

$$E = \frac{U_{needle}}{d} = 4 \cdot 10^9 \frac{V}{m} \tag{2.11}$$

Through the field strength at the tip of the needle a dust grain receives its final charge of about 10^5 positive electron charges ($\cong 2 \cdot 10^{-14}$ C) and is directed out of the dust source and into the beam line where it is accelerated by the 2 MV potential [Mocker, 2011].

In order to charge dust particles they have to be of conductive material. Common dust materials are iron, silver, copper or carbon. Lately a method to metal coat low-density silicate dust particles has been developed and so provide a chance to accelerate naturally insulating particles [Hillier et al., 2009].

2.1.3 Focusing

As charged particles are deflected by electric fields, the dust accelerator uses this principle to focus the dust beam. The position sensitive detector described in this thesis can help to monitor the focussing. As it determines the trajectories of individual dust particles the focus can then be analysed and improved from the statistics of the particle positions.
Similar to an optical lens a non-linear electric field deflects charges. Two cylindrical tubes in the dust accelerator's beam line at different potentials cause curved equipotential surfaces. In case of an increasing potential ($\Phi_2 > \Phi_1$) in the trajectory of the dust particles the defocussing effect of the electrostatic lens is predominant and thus the beam is scattered. In the dust accelerator the potential decreases ($\Phi_2 < \Phi_1$) and so the lens is focusing [Mocker, 2002].

2.2 Position Detector

The dust accelerator's beam line includes a position sensitive detector. The purpose of this detector is the monitoring of the horizontal and vertical displacement from the central beam line of individual dust particles. Depending on the position of the particle a charge is induced on conductive plates, which can then be amplified and analysed without influencing the particle's motion. The position detector uses the principle of induction to determine the dust particle's location in the beam line. This section describes the physical principles and the design of the position sensitive detector.

2.2.1 Electrical Induction

A metal as a conductor has a constant potential. Thus electric charges inside a metal are acted upon by forces induced by an electrical field. If a charged particle approaches a metal plate the free electrons in the metal move due to the force induced by the particles electric field in order to reach a state of equilibrium.

This movement of inner free electrons is called induction. The result of induction is that the metal plate functions as a shield for electric fields. The electric field due to the induce charge opposes the applied field.
To understand the way in which free electrons behave when a conducting plate is exposed to an electric field one has to consider the relationship between the electric field $\vec{E}$ and potential φ as a function of position $\vec{r}$:

$$\vec{E}(\vec{r}) \;=\; -\,\nabla\,\varphi(\vec{r}) \tag{2.12}$$

This relationship, when applied to the Maxwell equation for stationary electric fields

$$\begin{aligned} div\;\vec{E}(\vec{r}) \;&=\; \frac{1}{\epsilon_0}\,\rho(\vec{r}) \\ rot\;\vec{E}(\vec{r}) \;&=\; 0 \end{aligned} \tag{2.13}$$

yields the Poisson equation

$$\Delta\,\varphi(\vec{r}) \;=\; -\,\frac{1}{\epsilon_0}\,\rho(\vec{r}) \tag{2.14}$$

where ϵ_0 is the electric dielectric constant and ρ the electric charge density. Considering an infinite conductive plate lying in the xy-plane the electric charge density can be converted to a surface charge σ on the plane. Thus Eq. 2.13 can be written as

$$\vec{E}(\vec{r}; z=0) \;=\; \frac{1}{\epsilon_0}\,\sigma(\vec{r}; z=0). \tag{2.15}$$

Assuming a point charge $\rho(\vec{r}) \;=\; Q\,\delta(\vec{r}-\vec{r_0})$ with $\vec{r_0}$ as the location of the point charge, Eq. 2.14 has the solution

$$\Delta\,G(\vec{r},\vec{r_0}) \;=\; -\,\frac{Q}{\epsilon_0}\,\delta(\vec{r}-\vec{r_0}) \tag{2.16}$$

where G is the Green's function of the Laplace operator Δ:

$$\Delta\,G(\vec{r},\vec{r_0}) \;=\; -\,\frac{1}{4\pi\epsilon_0}\,\frac{1}{|\vec{r}-\vec{r_0}|} \;+\; f(\vec{r},\vec{r_0}) \tag{2.17}$$

with $f(\vec{r}, \vec{r_0})$ is an arbitrary symmetrical function in $\vec{r}$ and $\vec{r_0}$ that fulfils the Dirichlet boundary condition that expects $G(\vec{r}, \vec{r_0}) \equiv 0$ on the conductive plate

$$\Delta f(\vec{r}, \vec{r_0}) = 0. \tag{2.18}$$

Under these constraints $f(\vec{r}, \vec{r_0})$ appears to be the charge density of an image charge on the other side of the conductive plate. The sum of the charge and image charge solve the Poisson equation (2.14). Thus the potential $\varphi(\vec{r})$ of a charge in front of a conductive plate at distance $\vec{r_0}$ is given by

$$\varphi(\vec{r}) = \frac{1}{4\pi\epsilon_0} \left(\frac{Q}{|\vec{r} - \vec{r_0}|} + \frac{Q^{im}}{\left|\vec{r} - \vec{r_0}^{\,im}\right|} \right) \tag{2.19}$$

Using the Dirichlet boundary condition this leads to the conclusion that the potential φ on the conductive plate equals zero which gives

$$Q^{im} = -Q; \quad \vec{r_0}^{\,im} = -\vec{r} \tag{2.20}$$

The electric field on the plate can then be determined by Eq. 2.12

$$\begin{aligned} \vec{E}(\vec{r}; z = 0) &= \frac{Q}{4\pi\epsilon_0} \left(\frac{(x, y, z - z_0)}{|\vec{r} - \vec{r_0}|^3} - \frac{(x, y, z + z_0)}{|\vec{r} - \vec{r_0}|^3} \right) \\ &= -\frac{Q}{2\pi\epsilon_0} \frac{z_0}{(x^2 + y^2 + {z_0}^2)^{3/2}} \vec{e_z} \end{aligned} \tag{2.21}$$

where $\vec{e_z}$ is the unit vector in the z direction perpendicular to the conductive plate. Thus the induced surface charge $\sigma(\vec{r})$ in Eq. 2.15 is given by

$$\begin{aligned} \sigma(\vec{r}) &= \epsilon_0 \vec{E}(\vec{r}; z = 0) \\ &= -\frac{Q}{2\pi} \frac{z_0}{(x^2 + y^2 + {z_0}^2)^{3/2}} \end{aligned} \tag{2.22}$$

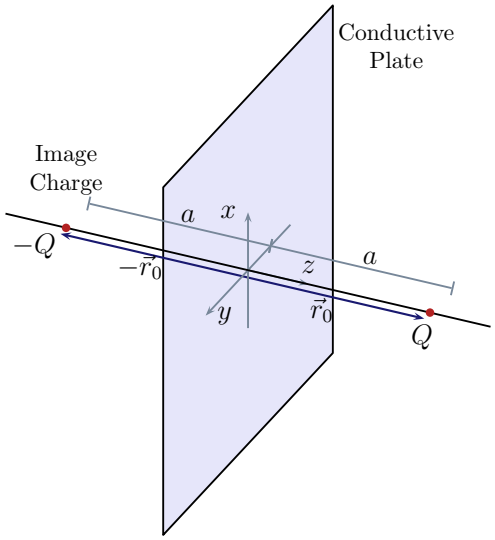

Figure 2.3: Principle of image charge (from *www.semibyte.de*[1])

The integral of the surface charge over the entire conductive plate is consequently:

$$\begin{aligned} Q^{induced} &= \int_{z=0} \sigma(\vec{r})\, dx\, dy \;=\; \int \sigma(\vec{r})\, \rho\, d\rho\, d\varphi \;=\; \int 2\pi\sigma(\vec{r})\, \rho\, d\rho \\ &= -\,Q \int \frac{z_0}{(\rho^2 + {z_0}^2)^{3/2}}\, \rho\, d\rho \\ &= -\,Q \end{aligned} \tag{2.23}$$

To simplify matters the integral was transferred into polar coordinates by using the identity $dx\, dy = \rho\, d\rho\, d\varphi$ with $\rho = \sqrt{x^2 + y^2}$. Equation 2.23 shows that the surface charge induced on the infinite conductive plate equals the image charge [Nolting, 1997].

2.2.2 Charge Between Two Parallel Plates

[1] *http://semibyte.de/dokuwiki/nat:graphiken:physik:methode_der_spiegelladung*

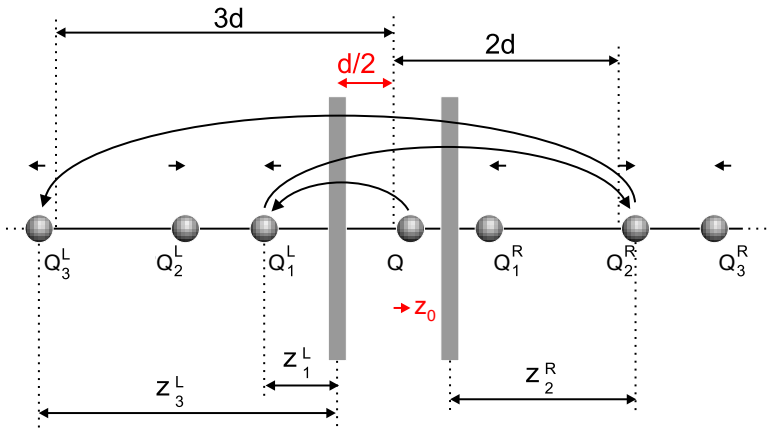

Figure 2.4: A charge between two conductive plates induces a series of image charges. (Based on a sketch from Winters et al. [2006]).

The position detector uses two parallel conductive plates and measures the induced charge on one of the plates by a passing dust grain. The particle moves parallel to the detector plates through the assembly. The surface charge is dependent on the distance $\vec{r_0}$ of the charge to the plate as shown in Eq. 2.22. Between two conductive plates the induced charge on one plate is no longer the charge itself with reversed sign (e.g. Eq. 2.23) but includes the effect of the second plate.

The image charge of a charged particle induced in one plate induces another image charge in the other plate. This image charge again induces an image charge in the first plate and so on. Thus a series of image charges is induced. Figure 2.4 illustrates this.

The charge Q is between two parallel conductive plates separated by a distance d and is located at a distance of z_0 from the center between the plates. Q induces an image charge ${Q_1}^L$ in the left plate. This image charge induces another image charge ${Q_1}^R$ in the right plate which then induces a third image charge in the left plate again and so on as indicated by the arrows. The same procedure has to be applied to the right plate too. The sum of all image charges on one side gives the induced surface charge on the plate.

The absolute distance of all image charges ${Q_n}^L$ on the left side of the plates and the distance of all image charges ${Q_n}^R$ on the right side of the plates is given by ${z_n}^L$ and ${z_n}^R$ respectively:

$$\begin{aligned} {z_n}^L &= (2n-1)\frac{d}{2} - z_0(-1)^n \qquad \text{distance to the left plate} \\ {z_n}^R &= (2n-1)\frac{d}{2} + z_0(-1)^n \qquad \text{distance to the right plate} \end{aligned} \tag{2.24}$$

In the detector the conductive plates on which the charge will be induced are not infinite as assumed in Section 2.2.1. Thus in Eq. 2.23 the integral can not be taken over the entire plate but is limited by the actual plate size R.

$$\begin{aligned} Q^{induced} &= -Q \int_0^R \frac{z_0}{(\rho^2 + {z_0}^2)^{3/2}}\, \rho\, d\rho \\ &= -Q \left(1 - \frac{z_0}{\sqrt{R^2 + {z_0}^2}}\right) \end{aligned} \tag{2.25}$$

Now the charges ${Q_1}^L$ and ${Q_1}^R$ can be calculated by the charges they were induced by and the distance to the plate [Winters et al., 2006].

$$\begin{aligned} {Q_n}^L &= -{Q_{n-1}}^R \left(1 - \frac{{z_n}^L}{\sqrt{R^2 + ({z_n}^L)^2}}\right) \\ {Q_n}^R &= -{Q_{n-1}}^L \left(1 - \frac{{z_n}^R}{\sqrt{R^2 + ({z_n}^R)^2}}\right) \end{aligned} \tag{2.26}$$

The sum of all charges on the left side gives the induced charge on the left plate and vice versa for the right plate. This has to be done numerically and produces the dependence shown in Fig. 2.5. The IDL code written for this calculation is given in Appendix B.1

These considerations are necessary to understand the functionality of the position sensitive detector. It is introduced and described in the following section.

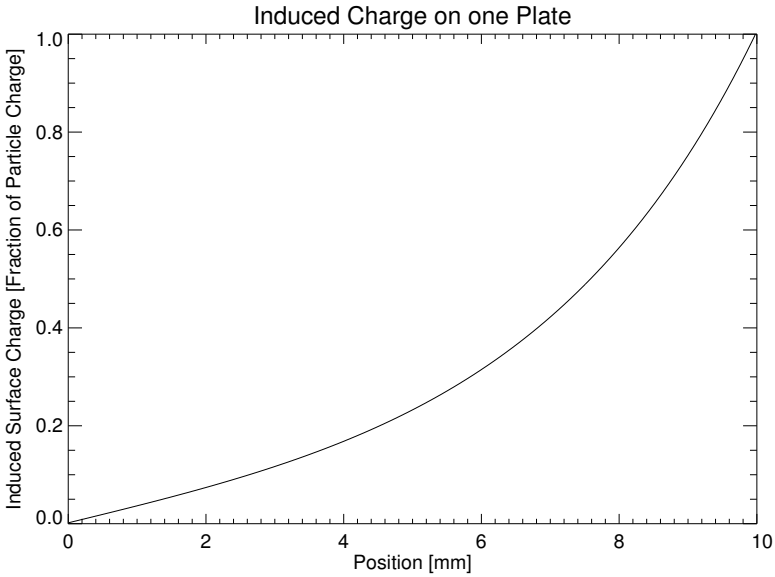

Figure 2.5: Relation of induced charge on one plate and distance given by the theory. The plate which carries the induced charge is located at 10 mm, the opposite plate at 0 mm. The number of considered image charges is 100.

2.2.3 Design of the New Plate Detector

The new position sensitive detector at the Heidelberg dust accelerator is based on a position detector described by Fechtig et al. [1978].

The new detector includes four pairs of copper printed circuit boards (PCB) of 26 mm times 38.75 mm area, separated by a distance of 15 mm. The pairs are perpendicular to the neighbouring pairs so that a dust particle's offset from the central axis can be detected in every direction. One plate of each pair is grounded, the other one is connected to a common charge amplifier. The pairs are separated by copper panels to shield each pair from the others. The panels are 5 mm wide and have a 10 mm round opening for the dust grains to pass through, resulting in a total length of 185 mm as illustrated in Fig. 2.6.

A charged dust particle that flies through this set up induces charge on the copper of the PCB that is higher the closer the particle passes the measuring plate (Section 2.2.1). The signal can be recorded by one channel of the oscilloscope and the position of the particle relative to the plates is derived by the relative

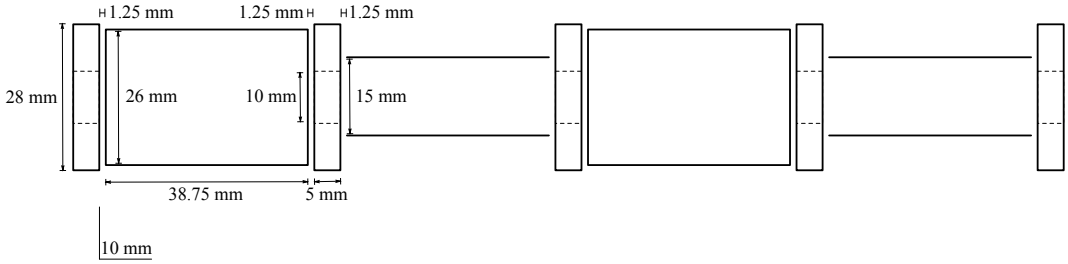

Figure 2.6: Side view of the detector with measurements. The sketch is drawn to scale as indicated by the scale bar.

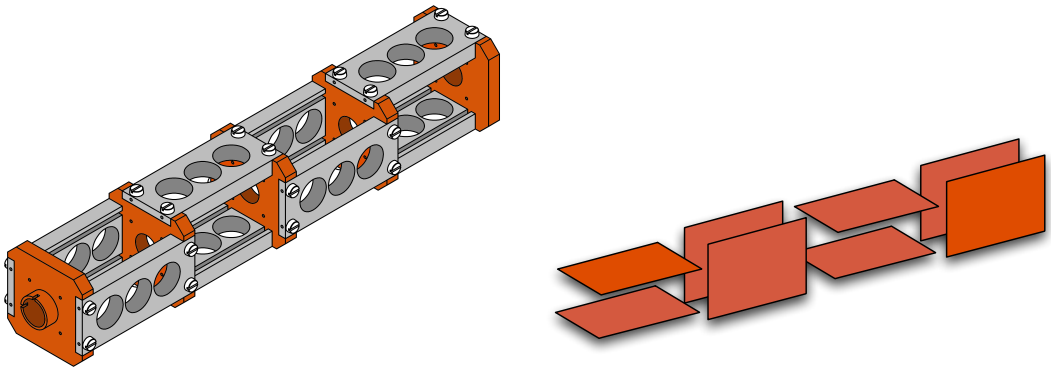

Figure 2.7: Rack of the position sensitive detector (left). Grey symbolises PEEK, red copper. The detecting plates are placed perpendicular to the PEEK plates as shown in the right sketch.

heights of the sequence of signals.

The left part of Fig. 2.7 shows the design of the rack of the position sensitive detector. The right part of Fig. 2.7 illustrates the adjustment of the detecting PCB pairs which are placed in the grooves of the PEEK[2] frames. A little rim of 1.25 mm on each side of the conductive plate prevents the contact to the grounded copper panels.

The detector is shielded by a 218 mm long and 72 mm wide copper cylinder that surrounds it such that the detector is inside a Faraday cage that keeps external

[2]Polyether ether ketone (PEEK) is a non-conductive organic polymer that is compatible with vacuum conditions.

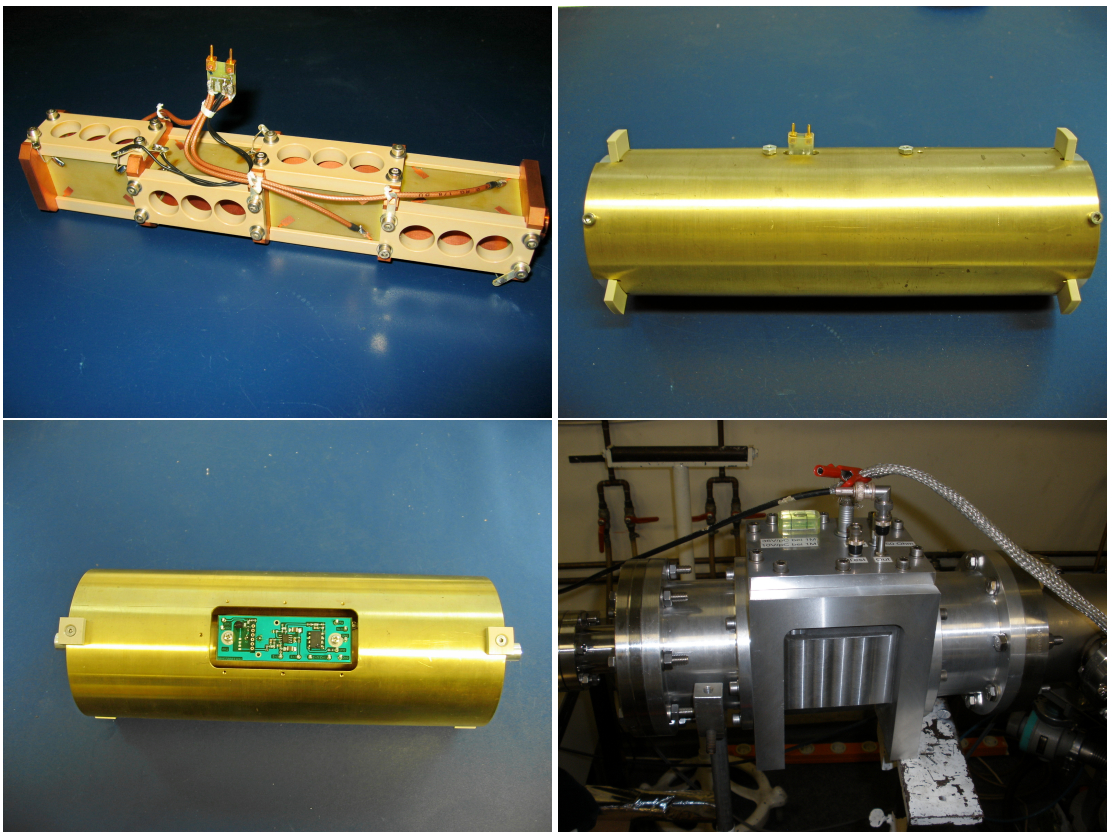

Figure 2.8: From left to right and top to bottom: The detector, inner shield with plug to the charge amplifier, outer shield with charge amplifier and the housing attached to the dust accelerator's beam line.

electric fields from affecting the detector. The charge amplifier devices are attached on top of the cylinder. A second copper cylinder surrounds the inner one with an opening for the amplifier to be attached to an external battery power supply. This prevents disturbance from the alternating voltage of common supplies. The ends of the cylinder are screened by conductive meshes for further shielding. This set up is placed into an aluminium housing for attachment to the beam line of the dust accelerator. The housing has a lid for easy access to the charge amplifier. Figure 2.8 shows the detector and shields.
There is a test input to the detector and one output that carries the amplified charge signal. The test input allows the detector to be supplied with a well char-

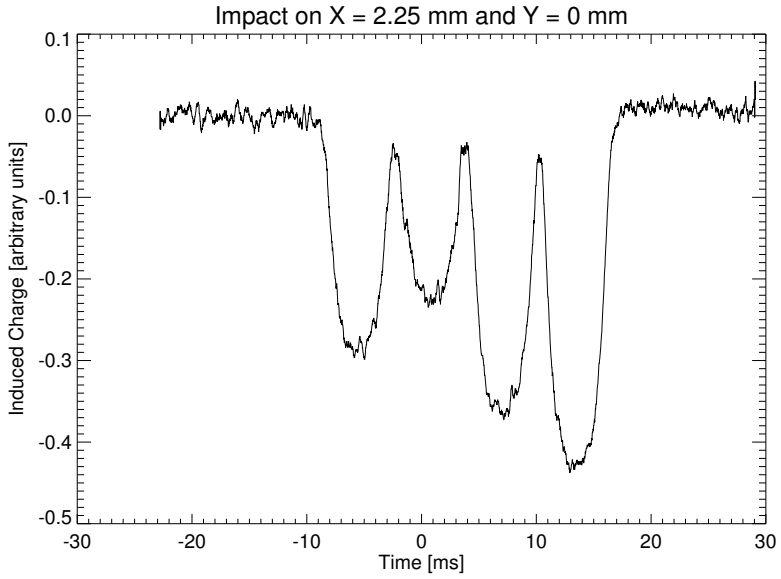

Figure 2.9: An example of a signal produced by the position sensitive detector.

acterised signal for checking the functionality of the detector without the need for charged particles flying through it. This test was performed before installing the detector in the beam line.

A signal produced by a particle traversing the position sensitive detector shows four charge peaks in which the first and third give information about the horizontal position of the passing particle and the second and fourth peak give information about the vertical position. Figure 2.9 shows an example of a recorded signal. This enables the detection of the position of a particle with one amplifying device only. The total amount of charge is not needed to calculate the position. The position can be determined by knowing only the amplitude ratios and these ratios remain constant for different amounts of charge.

In the detector assembly it is assumed that a particle passes the detector parallel to the electrode plates. This assumption is mostly valid even though a particle trajectory does not necessarily has to be parallel. A simple consideration explains the effect. The detector is placed approximately 5 m behind the dust source. The radius of the position detector's opening is 5 mm. Therefore, a detected dust particle needs to have an angle α given by $\tan(\alpha) = \frac{0.005m}{5m} = 10^{-3^{\circ}}$. For a small

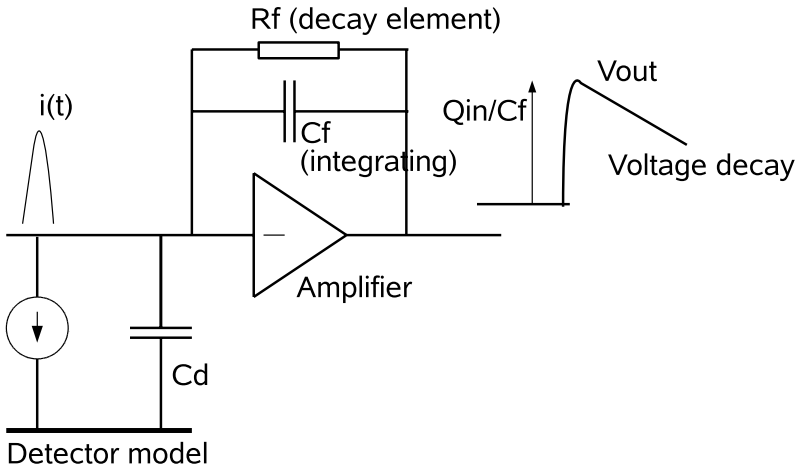

Figure 2.10: Sketch of a charge sensitive amplifier (from Srama and Auer [2008]).

angle $\tan(\alpha) \approx \alpha$ can be assumed. Thus the maximum angle of a particle is approximately represented by $10^{-3^{\circ}}$. For the detector with a length of 185 mm this leads to a displacement $d = \tan(\alpha) \cdot 0.185m = 185\mu m$. In this work the position of a particle is determined by a second independent measurement with a spatial resolution of 1 mm. Thus the effect of a particle's trajectory is small but has to be considered as a possible source of error.

2.2.4 Charge Amplifier

The advantage of the described position sensitive detector is that all four detecting plates are connected to the same charge amplifier, so that no further calibration of amplifying devices is necessary. One electrode of each electrode pair is connected to the common charge sensitive amplifier (CSA) while the counter electrode is grounded.
The detector uses an integrated Amptek model A250F/NF CSA with a rise time of 80 ns and has a bandwidth between 2 kHz and 10 MHz (Amptek datasheet). The amplifier is supplied by an external 6 V battery. This model converts a given charge into a voltage signal that can be recorded by an oscilloscope.

Figure 2.10 shows a sketch of the set up of the charge amplifier. A time dependent charge signal $i(t)$ produced by the detector passes through the operational amplifier and is looped back over a parallel resistor R_f and capacitance C_f. Thus the output voltage of the amplifier V_{out} decays with the time constant $R_f \cdot C_f$ and is given by $V_{out} = \frac{Q}{C_f}$. Because the preamplifiers try to keep the input node voltage unaltered, the charge Q is the same charge as the one induced on the detector but with reversed sign so that $V_{out} = \frac{-Q_{in}}{C_f}$ [Srama and Auer, 2008].
The resistance R_f and capacitance C_f in the amplifier feedback loop cause a drop of the converted charge to voltage signal, which decays with the time constant $R_f \cdot C_f$. Due to the unaltered voltage on the input node only alternating signals in a determined bandwidth can be amplified [Auer, 2011]. The detector was used with $R_f = 1$ GΩ and $C_f = 0.25$ pF resulting in a time constant of 0.25 ms. The fall of the signal due to this amplifying process can not be detected as the signals are too short even for slow particles. With a detector signal length of some tens of milliseconds also the overshoots due to the operational amplifier are easily lost in the noise and can be neglected.
The detector can be used with two different amplification factors: 10 V/pC or 36 V/pC. In the following experiments the 36 V/pC amplification was used. This means that a charge of 1 pC was converted to 0.028 V.

2.2.5 Other Position Detector Designs

The Heidelberg dust accelerator used a tube and wire position detector based on the principle of induction as described in Section 2.2.1 before the development of the new plate detector.
The tube charge detector consists of three tubes of each 50 mm in length with diameters of 10 mm. A particle flying through the set up first passes a tube that is separated along the trajectory of the particle in two equal half cylinders one connected to a charge amplifier, the other one grounded. A second half cylinder pair separated perpendicular to the first one is installed next, again one grounded and one half cylinder connected to a charge amplifier. The third cylinder is a

whole cylinder connected to a charge amplifier. The bottom left picture in Fig. 2.11 illustrates this. While the first two half cylinder pairs provide information about the position of a passing dust grain, the third cylinder detects the charge of the particle, which is necessary for understanding the position dependence of the induced charge signal on the half cylinders.

The detector is capable of detecting charges as high as the particle charge itself as almost no charge is lost to screening. Unfortunately this detector has not yet been calibrated. There are however simulations of the induced charge on the detector dependent on the particle position that show high sensitivity for trajectories around the centre [Srama, 2005].

The low charge detectors as described by Srama and Auer [2008] use the same principle but without determining the radial position of a dust grain with respect to the beam line axis. Each consist of one undivided copper cylinder of 15 mm length to measure the induced charge of a passing particle which is now equivalent to the particle's charge itself, see top picture in Fig. 2.11. The physical principle of this detector is further described in Section 2.2.1. These charge detectors are able to detect charges as low as 0.2 fC with a noise level of 0.15 fC under operational conditions [Srama and Auer, 2008].

Another position sensitive detector used at the Heidelberg dust accelerator uses four conductive wire pairs of 50 mm length. There are two horizontal and two vertical pairs perpendicular to the trajectory of the dust particle separated by a distance of 20 mm. For shielding it uses grounded panels between the wire pairs similar to the plate detector design. Again one wire is connected to a common charge amplifier while the other one grounded. The bottom right picture in Fig. 2.11 illustrates this. A passing dust grain induces a different amount of charge on the wires depending on the particle's distance to the detecting wire. Since the wires are only 1 mm in diameter only about 16 % of the particle charge is induced on each wire which limits the detector to only work for primary charges above 10 fC [Srama, 2005].

Thus the new position sensitive detector using plate pairs is an improvement on both former detector designs as it collects more charge then the wire detector and

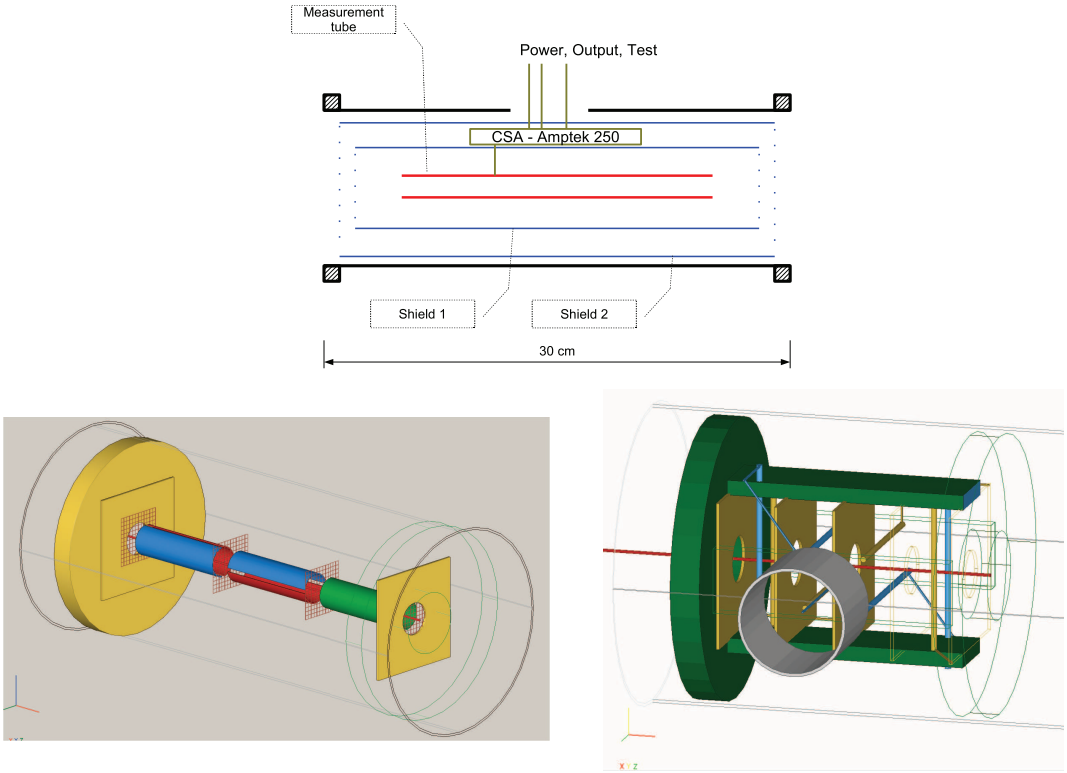

Figure 2.11: Sketch of the low charge detector developed by Srama and Auer [2008] (top) and simulation model of the tube (bottom left) and wire (bottom right) position detectors described by Srama [2005].

does not need the measurement of the total charge as does the tube detector.

2.3 Calibration Set Up

To obtain an independent position measurement for calibrating the position detector a target for locating a particle's impact charge was developed and installed in the beam line. The following section describes the functionality and briefly the physical principle behind this apparatus.

2.3.1 Impact Ionisation

A charged dust particle impact on a target produces ions and electrons that can be detected by charge amplifiers or multipliers.
Depending on an impacting particle's velocity two models of impact ionisation have to be considered. Low impact velocities below 5 to 10 km/s induce surface effects that include surface heating (up to 25000 K) by electron emission due to very high electric fields shortly before the impact. The electrons emitted from the target material are accelerated towards the dust particle and ionize atoms in the particle's surface and stimulate their desorption [Sysoev et al., 1997].
Higher impact velocities up to 100 km/s result in the ionisation of the particle and target by shock waves. Owing to the very high pressure (up to 10^8 atmospheres) and temperature (several hundred thousand degrees) resulting from the collision of the grain and target material a plasma develops and expands around the point of impact [Hornung et al., 1996].
The ions and electrons produced in either process can be accelerated by applied electric fields and detected by charge multipliers. This principle is used in time of flight mass spectroscopy in which the different ions are distinguished by their different times of flight due to their masses. However the experiment in this work used a charge amplifier on the target to detect the ions and electrons produced by the impact. Figure 2.12 shows an example charge signals on a silver target impacted by iron nickel dust grains for low and high impact velocities [Mocker, 2011]. The high velocity impact produces about 25 times more impact ions than the low velocity impact. The dip at low velocities shortly before the charge rise is due to the particle's image charge induced on the target.
The impact produces a cloud of impact plasma ions and electrons that expands. As the ions and electrons in the plasma are able to move freely like electrons in a conductor the surface plasma ions and electrons are shielding the inner charges from outer electric fields. This is called Debye shielding. After the expanding plasma cloud has reached the critical dimensions so that the Debye length, which describes the shielding length at which the outer electric field is reduced to $1/e$, is equal to the dimension of the plasma the surface shielding is inefficient and

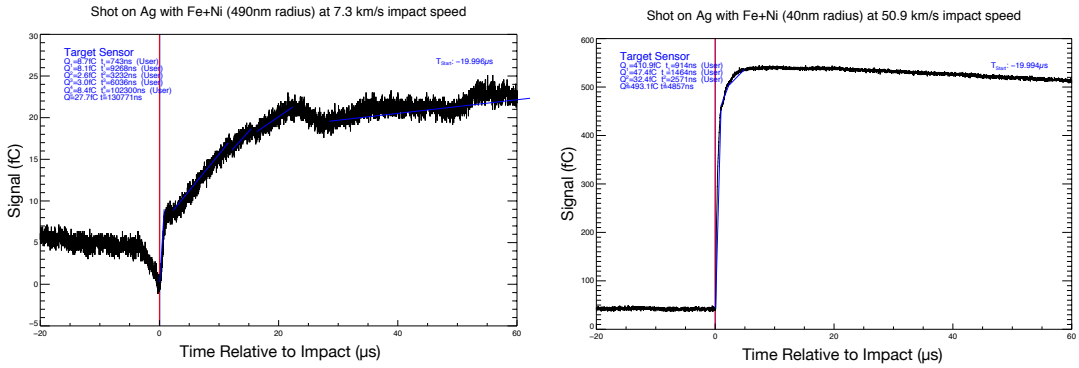

Figure 2.12: Charge signals for low (left) and high (right) impact velocities from shots of iron nickel particles on a silver target (from Mocker [2011]).

the outer electric field can enter the plasma and accelerate the ions and electrons [Freidberg, 2007]. Thus when the plasma becomes transparent to an applied field, the charges can be accelerated onto a detector, for recording.

2.3.2 Calibration Principle and Assembly

The position sensitive detector is able to produce signals that are dependent on a dust particle's location perpendicular to the beam line. To calibrate the detector a reference measurement was designed that gives the position of the particle independently from the position detector itself.

To obtain an independent position measurement target plates were designed that contain separate conductive segments. Each segment was attached to a charge amplifier. The target was placed directly after the position detector so that a dust particle, after passing the position detector, impacts on a target plate. If the particle impacted on one of the conductive segments the impact ions and electrons were amplified by the charge amplifiers and seen on the oscilloscope. Thus by knowing the size and location of the area that responded to the impact the dust particles position could be determined independently from the position detector.

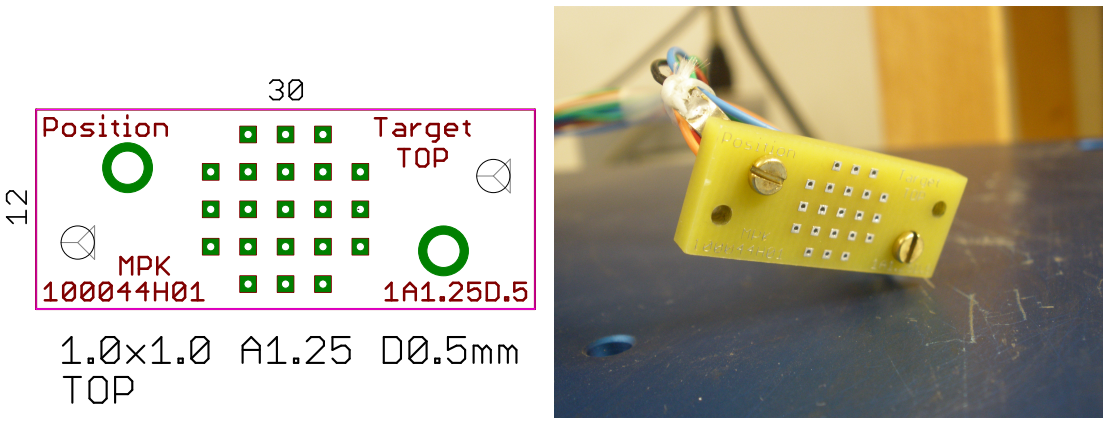

Figure 2.13: Technical drawing of the front side of the impact target (left) where each small square is a separate conductive electrode and the target plate with cables (right).

Eight different designs of 30 mm times 12 mm target plates with different conductive segment sizes and distances were designed. The goal was to be able to measure as many positions as precisely as possible. Unfortunately, due to limited time constraints only one target was used.

The target plate (Fig. 2.13) had square impact segments of 1 mm side length separated by a distance of 1.25 mm on the front side of the plate. The charge amplifiers ware attached to the rear of the target and connected to the conductive segments via holes. The holes, 0.5 mm in diameter, were soldered up so that dust particles were not lost through them.

This method produced small concave tubular target regions which may have helped confine the impact plasma, reducing the signal on neighbouring target segments. The plates and thus the tubes had a thickness of 3.2 mm in order to trap the impact plasma efficiently. There were 21 impact segments symmetrically distributed around the centre of the plate. Each impact segment was fixed to a connector which was attached to the vacuum flange. Figure 2.13 shows the technical drawing of the impact plate and a picture with the connection cables to the flange.

In order to get a definite impact signal a grid of 70 % transmission was adjusted between the detector and the target with a distance of 36.5 mm to the detector

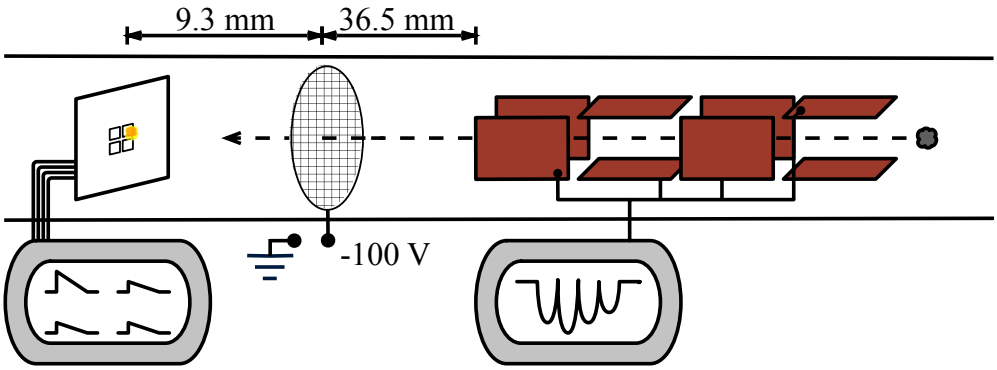

Figure 2.14: Sketch of the calibration assembly.

and 9.3 mm to the plate. A negative 100 V bias voltage was applied to the grid while the impact segments were grounded, so that negative ions and electrons that are produced by the impact of the dust particle on the target were collected by the impact segments.

The flange had twelve connections, one of which was used for the bias voltage of the grid. Outside the vacuum chamber six charge amplifiers were fixed to the flange connections. Due to the limited number of charge amplifiers and oscilloscope channels only six impact segments' signals could be recorded at once. The amplified charge signal was recorded on two oscilloscopes.

In case of a dust particle impacting one of the metal-coated segments a clear signal was expected while an impact on the non-coated segment should produce weak signals on each segment connected to a charge amplifier. Figure 2.14 shows a rough sketch of the calibration assembly applying an impact target with only four segments for clearness.

3 Measurement and Simulation

3.1 Experimental Measurement

Calibration of the position sensitive detector requires a second independent reference. For this several segmented impact targets were designed and installed behind the detector.

The dust accelerator was used at a voltage of 1.8 MV to accelerate polypyrrole (PPy) coated olivine dust. Particles with speeds of 3 km/s or larger were selected for the experiment to filter out too low charged particles.

For each dust particle that showed impact features on the target segments the detector signal, a reference charge detector signal and the impact signals of all six connected segments were recorded. By adjusting the steerer and focus voltages in the accelerator, the dust beam's centre could be moved to hit the target's connected segments efficiently.

Owing two the limited number of charge amplifiers, the charge amplifiers had to be switched between different target segments. First a total of 225 impacts were recorded for the bottom right part of the beam line. In a second measurement 263 signals were recorded for the top left part of the beam line. Table 3.1 lists the locations of the measured impact segments. Figure 3.1 plots their position.

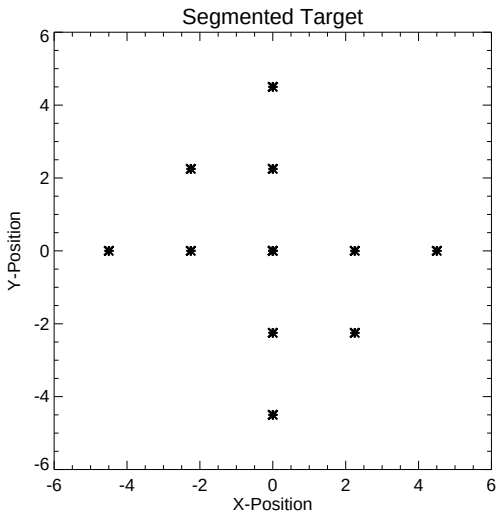

Figure 3.1: Location of the connected impact segments in the beam line.

Table 3.1: List of connected impact segments.

X-Position [mm]	Y-Position [mm]	Y-Position [mm]	X-Position [mm]
0	0	0	0
	2.25		-2.25
	4.5		-4.5
2.25	0	2.25	0
	2.25		-2.25
4.5	0	4.5	0

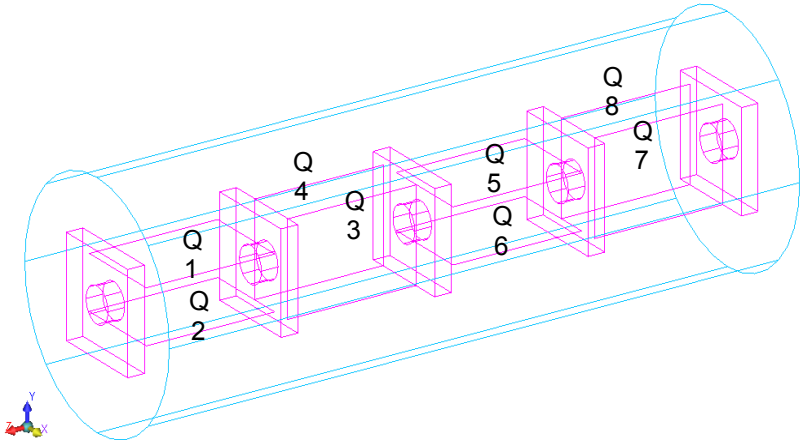

Figure 3.2: Set up used for the simulation.

3.2 Simulation of Detector Performance

In addition to the experimental set up a simulation of the position sensitive detector with the software package COULOMB [2011] was obtained. This programme allows the user to simulate the electric field lines of an apparatus in 3D and produces the induced charge by a numerical solution of Eq. 2.15. With a simulation like this the ideal detector signals can be calculated and compared to the real signals. The simulation was calculated by Jianfeng Xie and Dr. Zoltan Sternovsky from the Laboratory of Atmospheric and Space Physics at the University of Colorado at Boulder.

The position sensitive detector set up was modelled in this programme as shown in Fig. 3.2. The detector plates have a size of 26 mm times 38.75 mm and a separation distance of 15 mm. In addition to the detector (pink) the inner shielding cylinder (blue) was considered for the simulation (diameter of 70 mm). Q_1 to Q_8 indicate the plates of the detector for which the induced charge was calculated. Five grounded copper shields with apertures separate the plate pairs from each other. For the dust particle a point charge was assumed. The centre of the detector is located at (0,0,0).

In contrast to the real detector the outer shield and beam line were neglected.

Also the screens before and after the detector were neglected as they are should not change the results significantly in the ideal conditions of the simulation. The spatial extension of the dust grain was neglected in this simulation as it is not supposed to change the induced charge amount.
The particle charge was set to $Q_{particle} = 1$ so that induced charges can be read directly as fractions of the particle charge. The motion of the charge along the detector in the z direction was separated into 191 steps. Thus for every millimetre the induced charge could be calculated for each plate. By adding the different induced signals for the four plates the same way as how the charge amplifier was connected in the real detector set up the actual a detector signal could be simulated. Thus Q_1, Q_4, Q_6 and Q_7 were added.
The induced charge signals for different trajectories were calculated. Table 3.2 lists these and shows the location relative to the centre of the detector. Figure 3.3 plots the locations. In order to get a general horizontal and vertical dependence of the signal, the trajectories along the x- and y-axis were calculated. In addition the trajectories that match the target's impact segments were calculated as well. The target segment at x = 4.5 mm and y = 4.5 mm was considered in the simulation in order to examine an extreme trajectory even though this position does not exist in the real device because a particle with this displacement would hit the shields.

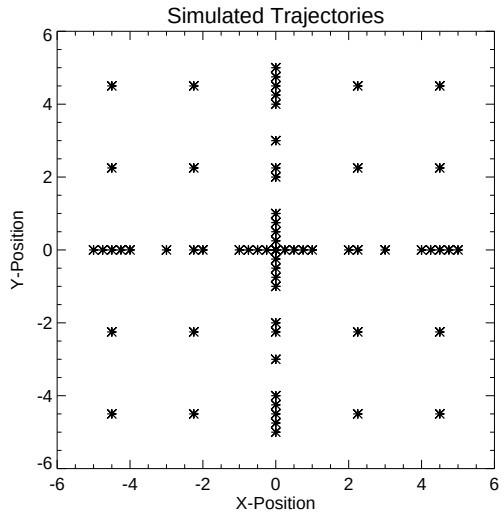

Figure 3.3: Overview of x- and y-positions of the simulated trajectories.

Table 3.2: List of simulated trajectories.

X-Position [mm]	Y-Position [mm]	Y-Position [mm]	X-Position [mm]
0	0	0	0
	± 0.25		± 0.25
	± 0.5		± 0.5
	± 0.75		± 0.75
	± 1		± 1
	± 2		± 2
	± 3		± 3
	± 4		± 4
	± 4.25		± 4.25
	± 4.5		± 4.5
	± 4.75		± 4.75
± 2.25	0	± 2.25	0
	± 2.25		± 2.25
	± 4.5		± 4.5
± 4.5	0	± 4.5	0
	± 2.25		± 2.25
	± 4.5		± 4.5

4 Results

4.1 Experimental Results

This section describes the results of the experiments that led to the correlation of the position detector signals and the position of a dust grain in the beam line. It also gives an idea of how accurate the detector is depending on noise and particle charge.

4.1.1 Detector Signals

Figure 4.1 shows four example detector signals for different speeds and charges of the passing dust grain. The speed of a particle can directly be determined from the signal length l in μs. As the detector is 185 mm wide the speed v is given by $v = \frac{185}{l}$km/s.

Note that the four amplitudes are troughs as the charge amplifier converts the signal. In between these four amplitudes, there are three peaks where the shielding is located. In general a signal is smoother the slower it passes the detector and thus the more the particle is charged (see Section 2.1.1). With a higher particle charge more charge is induced on the detector plates and thus the signal to noise ratio becomes larger.

The example signals in Fig. 4.1 show another interesting feature. The further the particle trajectory is displaced from the centre, which is represented by a great amplitude ratio, the closer the induced charge between two plate signals (the three peaks between the four troughs) approaches the base line. Each shielding panel has a 10 mm round aperture. A particle with a trajectory closer to the aperture's wall experiences the effect of the panel's shielding more efficiently. This is, because the induced surface charge σ on the panel increases with decreasing distance r to the panel ($\sigma \propto \frac{1}{r^2}$) (see Eq. 2.22). Thus fewer electric charge is induced on the plates that result in the signal when the particle is passing the shielding panels and the peak between two amplitues approches the base line.

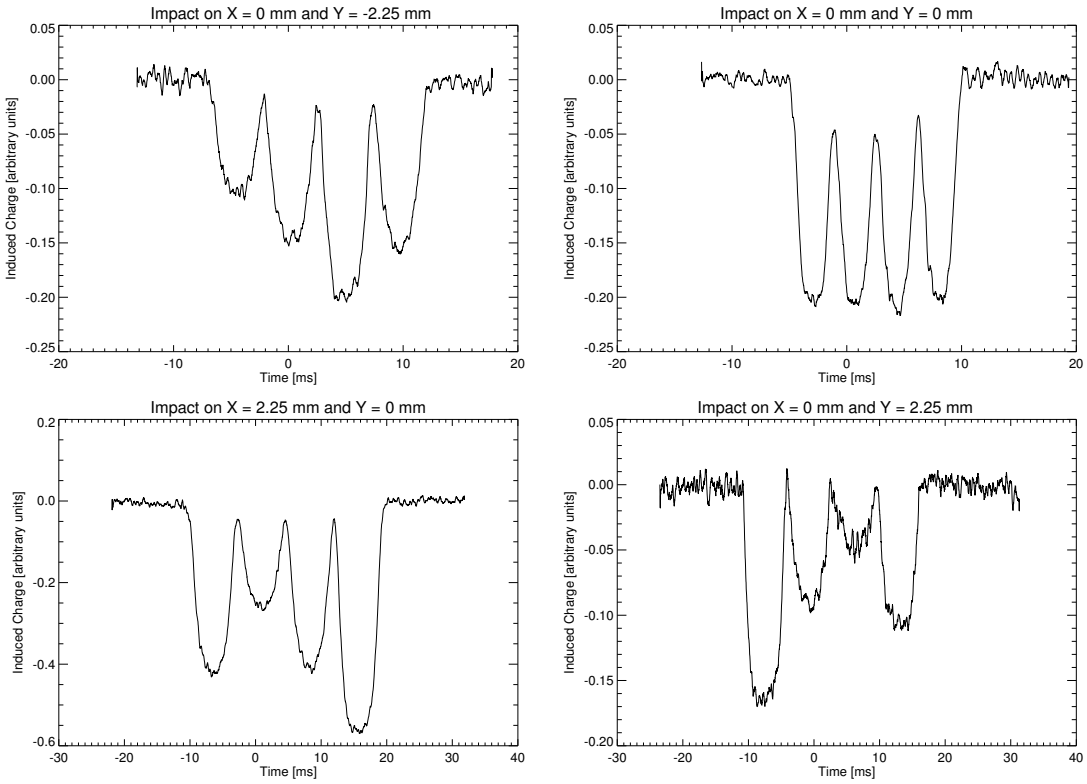

Figure 4.1: Sample detector signals for various particle charges, speeds and positions. The amplitudes are named A_1, A_2, A_3, A_4 with increasing time.

4.1.2 Data Evaluation

As described in Section 3.1 the position detector signal and impact signals were recorded for a dust grain impacting one of the connected segments on the target. The position sensitive detector signals were evaluated by determining of the four signal amplitudes A_1, A_2, A_3, A_4 relative to the base line. A self-developed IDL-based software programme working with the Canny edge detection algorithm [Canny, 1986] to find the amplitudes was programmed for this purpose. Additionally, the programme allows the user to subtract linear disturbances on the signal manually. The software instructions are given in Appendix A.1.
For each recorded set of impact signals the heights of the six impact charge signals were determined with another self-developed IDL-based software programme

working with the Canny edge detection algorithm [Canny, 1986] to find the impact time and the charge rise. The main functions of the code are given in Appendix B.2 and B.3 and the instructions are given in Appendix A.2.

Usually an impact produces signals on each segment, as the expanding charge cloud after the impact can spread over multiple segments before being affected by the electric potential applied to the segments. A charge signal was considered to be a direct impact on one of the segments when it was three times larger than the next highest signal. The value of three can be justified by the assumption that the charge cloud is described by a Gaussian. The range of the variance is localised where the charge dropped to $1/e$. As a rough estimate this was simplified to 1/3. Thus for the first measurement 39 signals out of 225, and for the second 104 signals out of 263, were considered to be direct impacts.

For some segments of the impact target this condition was too strict to obtain enough data points, thus some segments were not hit at all. Table 4.1 shows how many impacts for each target were used for the calibration described in the following section. The centre of the beam line at x = 0 mm and y = 0 mm was connected in both measurements and thus lists two values.

In order to get a general overview of the impacts and the corresponding detector signals ratio A_1/A_3 were plotted against ratio A_2/A_4 of the impacts that were judged to have hit a segment. As ratio A_2/A_4 provides information about the

Table 4.1: Number of impacts on target segments.

X [mm]	Y [mm]	Number of Impacts	Y [mm]	X [mm]	Number of Impacts
0	0	21 + 13	0	0	21 + 13
	-2.25	6		-2.25	12
	-4.5	0		-4.5	2
2.25	0	12	2.25	0	29
	-2.25	0		-2.25	33
4.5	0	0	4.5	0	15

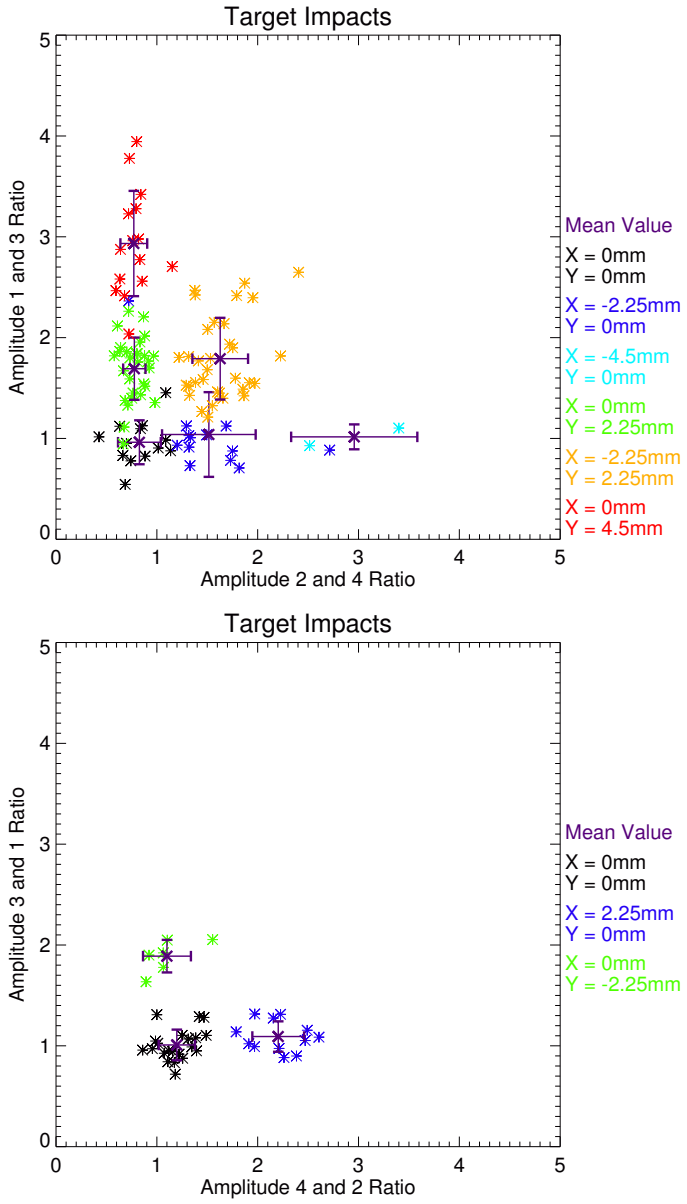

Figure 4.2: Amplitude ratios for the upper left (top) and bottom right (bottom) part of the impact target. The impact clusters represent the impact segments. The mean value of each cluster and its deviation are also shown. Note that the ratios in the second plot are inverse for consistency.

x-position and ratio A_1/A_3 about the y-position of the passing dust particle the impact positions can be seen as an accumulation of ratio signals. Figure 4.2 shows the resulting plots. The different coloured clusters represent the segments of the impact target.
The ratios are plotted in different colours for different impact segments in two plots with reversed amplitude ratios. This helps to visualize the similarity. A trajectory with a positive x value gives an A_4/A_2 value greater than 1 while a similar trajectory with a negative x value gives the inverse of that ratio. Thus the amplitude ratios in the two plots are inverse to show the symmetry of the detector. If a particle passes through the centre of the detector all four signal amplitudes ideally have equal heights. Hence, the ratios are 1. In the plot the black clusters represent the centre of the detector with amplitude ratios of 1.
In addition to the impact ratios the mean values and the standard deviations of each impact segment's data points were also plotted. The standard deviation in Fig. 4.2 becomes larger with larger amplitude ratios. This is equivalent to larger offsets of the dust particle from the centre of the detector. The larger deviation might be due to the fact that these particles have a trajectory that is not quite parallel to the detecting electrodes. This is necessary in order to reach the segments. Another explanation is the unideal induction process for example by charge loss to the shielding.
It might look like the detector becomes less accurate for larger amplitude ratios, but this is only true for the accuracy of the amplitude ratios. It is not applicable to the accuracy of the position itself. A great deviation in the amplitude ratio yields a more inaccurate determination of the position for ratios close to 1 than for larger ratios. This is further explained in section 4.1.5.

4.1.3 Experimental Calibration Curves

Each of the amplitude ratios can now be plotted against their x- and y-position in the beam line giving two calibration curves that will make it possible to determine a dust particle's trajectory from the detector signal.

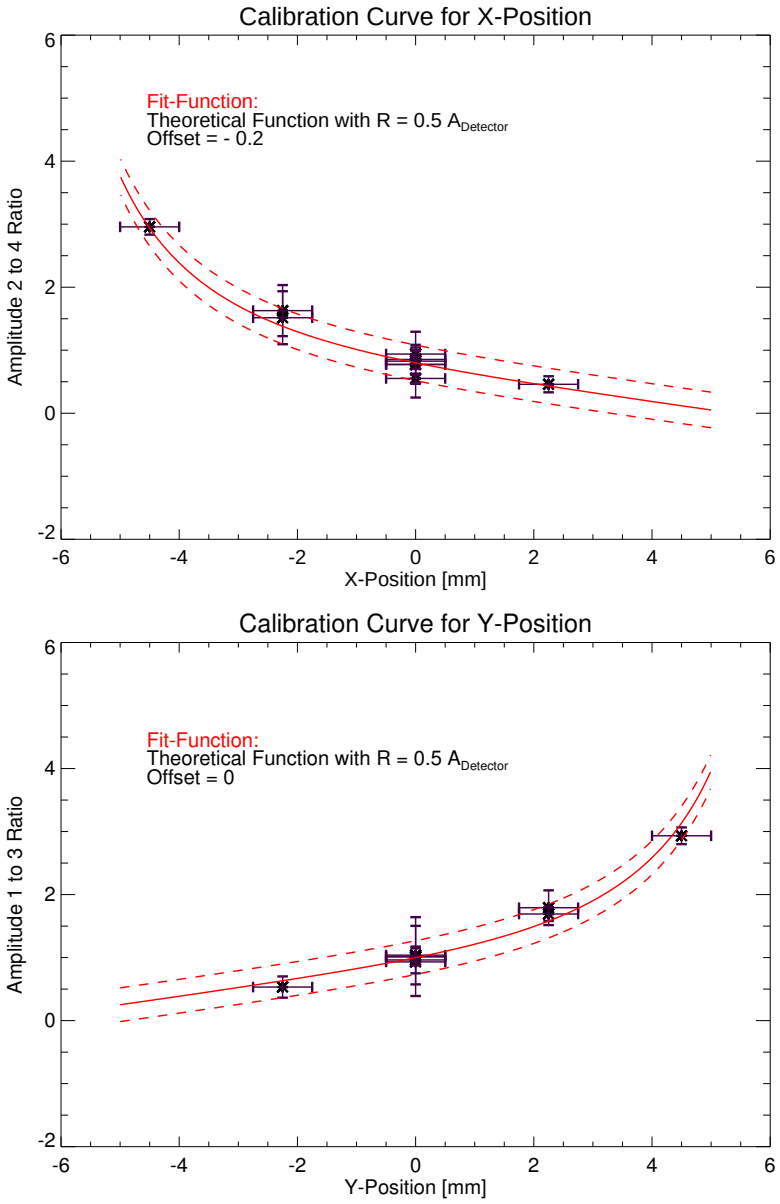

Figure 4.3: Calibration curve for horizontal (top) and vertical (bottom) position. The plot shows the correlation between the amplitude ratio and the position of a dust particle in the beam line. The fit (Appendix B.1), based on the two plates theory (Section 2.2.2), was adjusted by varying the apparent detector plate size R. The dashed lines symbolise the error curves.

Figure 4.3 shows the calibration curves for x- and y-position. For each horizontal and vertical segment location the amplitude ratios shown in Fig. 4.2 were plotted with their measured standard deviation. For position errors the dimension of the target segments (1 mm) were assumed. The measured amplitude ratios were fitted by a function based on the principle of induction between two finite plates as described in Section 2.2.2. The IDL code that was used to calculate the fit function is described in Appendix B.1. The mean of the data points' errors were calculated and used as errors of the curve. These error curves are added as dashed lines in the plots and are given by ± 0.28 for the horizontal calibration curve and ± 0.27 for the vertical calibration curve.

The fit function was adjusted by varying the plate areas while their distance was kept constant. The number of image charges that need to be summed in order to determine the induced charge on the plates was set to one hundred. In both calibration plots the induction function which uses half of the actual size of the real detector plates fits the data the best. Thus in an ideal set up without charge loss to the shielding or charge amplifiers the curve would describe a detector with plate sizes half the size of those in the real set up. This does not mean that only half of the charge is induced though as the surface charge decreases by a $\frac{1}{\rho^2}$ law with distance ρ (Eq. 2.22).

The calibration curve for the vertical positions does not show an offset to the theoretical function while the calibration curve for the horizontal positions has an offset of -0.2 in the amplitude ratio. This shows that the actual ratio is lower than in the idealized detector, which means that the charge induced on the plate that produces A_2 is too low or the charge induced on the plate that produces A_4 is too large when compared to a totally symmetric detector. This might be due to inaccuracies in the construction or installation in the beam line. The plates are all connected to the same charge amplifier with cables of different lengths. Thus their capacitance which has an effect on the charge amplification varies and might cause the offset. Nevertheless, the agreement of both calibration curve slopes indicates a high symmetry in the detector set up.

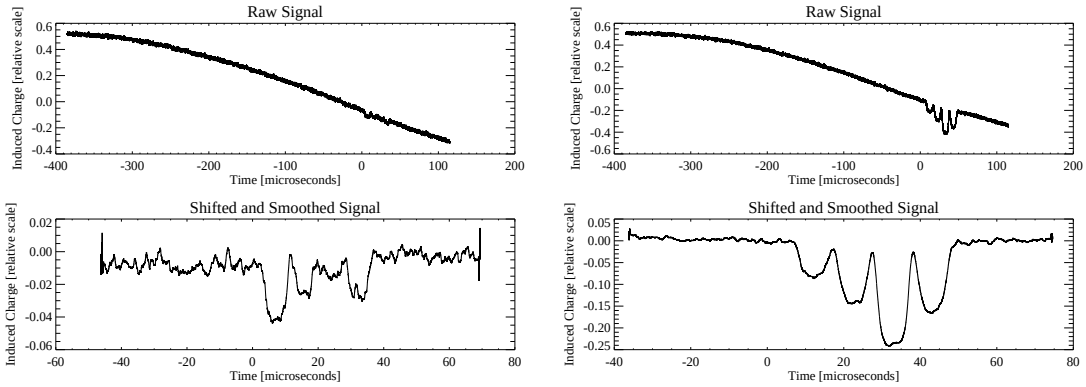

Figure 4.4: Signals with low signal to noise ratio (left) and high signal to noise ratio (right). The upper graph shows the raw signal recorded on the oscilloscope and the lower graph the shifted and smoothed signal processed by the software that was used for determining the amplitudes (Appendix A.1).

4.1.4 Noise and Disturbance

The determination of the amplitude ratios of the position sensitive detector is limited by different sources of error that are further discussed in this section.
The detector shows a sinusoidal function with a frequency of approximately 850 Hz on the oscilloscope. It was not possible to shield the detector from this disturbance, which is assumed to be caused by the turbo vacuum pump attached to the beam line. The evaluation software described in Appendix A.1 enables the subtraction of a linear baseline from the detector signal. It is possible to approximate the sinusoidal function as $sin(t) \approx t$ for small t. This method was used to subtract and shift the recorded detector signals.
The main factor of inaccuracy is due to the noise on the detector and charge amplifier. Noise can be produced by external electric fields inducing charge on the detector plates or inside the charge amplifier. Also the transmission to the oscilloscope can affect the signal. Owing to the double shielding the noise is relatively small, about (30.2±11.1) mV which corresponds to (1.11±0.41) fC charge noise on the detector. Section 4.1.6 explains how this noise level was determined.
Finally the reading inaccuracy has to be considered. This contributes to the accuracy of the amplitudes as they are determined manually. For relatively highly

charged particles the signal to noise ratio is large and the inaccuracy arises through poor determination of the amplitude's height. This error is relatively small in the order of the noise to amplitude ratio. Whereas for lower charged particles with a noise in the order of the amplitude itself it can be difficult to determine the amplitudes. Section 4.1.5 discusses the effect of the signal to noise ratio on the accuracy of the detector.
Figure 4.4 shows two original signals with different signal to noise ratios and their shifted and smoothed equivalents from which the amplitudes were determined. The signals were smoothed over 10 data points which means that the mean value of each interval was determined and plotted. This makes it more graphic and therefore accurate to find the correct amplitude.

4.1.5 Position Accuracy

In this section the accuracy of the position measured by the detector and its dependence on noise and therefore on the reading accuracy is discussed.
The determination of the detector amplitudes is limited by the noise on the detector signal. Thus the detector shows different accuracies for different signal to noise ratios. For high signal to noise ratios the detector accuracy becomes larger than for low signal to noise ratios as the amplitudes can be determined more precisely. In general the lowest amplitude should not be smaller than three times the standard deviation of the noise to guarantee the acceptable identification of the amplitude. Of course this depends on the position of the particle in the beam line as a dust grain with a large offset from the centre induces both, a high and a low amplitude. Section 4.1.6 discusses the charge limit of the detector further.
To interpret the position accuracy of the detector with x and y displacement from the centre the calibration curves in Fig. 4.3 were used. The following considerations are derived from the vertical calibration curve, but can be easily adjusted to the horizontal curve. This is as the horizontal and vertical curves are described by the same function but differ by an offset. Starting from a certain amplitude ratio the position can be determined using the calibration curves (Fig. 4.3). With noise

in the signal, the amplitude ratio cannot be determined accurately any more, but leads to a ratio uncertainty in the order of the noise. This then results in an uncertainty in the position. For each amplitude ratio the resulting uncertainty in the position was determined for a certain noise level. The noise level was normalized on the amplitude sum to make the considerations independent of the charge on the particle. Thus the signal to noise ratio is the ratio between the sum of the amplitudes and the noise.
For example, if we consider the amplitude ratio A_1/A_3 and an absolute noise N_{abs}, the normalised noise N_{norm} is given by $N_{norm} = \frac{N_{abs}}{A_1+A_3}$. Note that N_{norm} is the inverse of the signal to noise ratio. The amplitude ratio of A_1/A_3 can vary due to the noise by

$$\frac{A_1 \pm N_{abs}}{A_3 \mp N_{abs}} = \frac{A_1 \pm N_{norm} \cdot (A_1 + A_3)}{A_3 \mp N_{norm} \cdot (A_1 + A_3)} = \frac{\frac{A_1}{A_3} \pm N_{norm} \cdot \left(\frac{A_1}{A_3} + 1\right)}{1 \mp N_{norm} \cdot \left(\frac{A_1}{A_3} + 1\right)}$$

This only depends on the amplitude ratio and is independent from the amplitudes themselves. There are two extreme cases. In the worst case the higher amplitude is misread as too high and the lower as too low (upper sign) and vice versa (lower sign). This leads to the maximum uncertainty due to the signal noise. The position inaccuracy based on this consideration is shown for different signal to noise ratios (${N_{norm}}^{-1}$) in Fig. 4.5. Instead of the amplitude ratio, the corresponding y-position is plotted to give a quantitative idea of the detector inaccuracy.
The signal to noise ratio is often given in dB. This logarithmic scale is used to show the ratio over broad ranges. The conversion is given by:

$$SNR = 10 \cdot \lg\left(\frac{A_{signal}}{A_{noise}}\right) dB = 10 \cdot \lg\left(\frac{A_1 + A_3}{N_{abs}}\right) dB$$

Figure 4.5 shows that the detector is most sensitive to inaccuracy due to noise when the particle passes through the centre of the detector. This can be understood as the ratio changes much more when two amplitudes are nearly equal than when when the amplitudes already have a large difference that leads to a high ratio. The symmetry in the curves represents the symmetry of the detector.

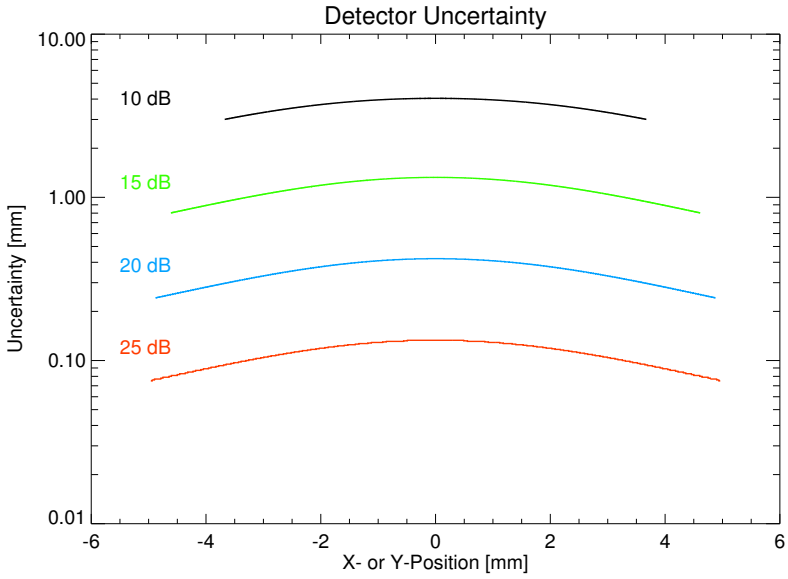

Figure 4.5: Detector uncertainty as a function of the displacement from the centre of the detector for different signal to noise ratios: 25 dB (orange) 20 dB (blue), 15 dB (green), 10 dB (black). In the same order the signal to noise ratio $\frac{A_{signal}}{A_{noise}}$ is given by 316, 100, 32 and 10.

There is no difference in the derived inaccuracy if the amplitude ratio considered is reversed. An A_1/A_3 ratio of 2 is the same as an A_3/A_1 ratio of $\frac{1}{2}$ and the detector is independent of which ratio is chosen due to its symmetry.
For the x-position the same result is valid but the curves are shifted in the negative x direction due to the -0.2 offset in the calibration curve, so that the maximum of all the dB curves occurs at x = -0.3 mm.
Figure 4.6 shows the maximum position uncertainty as a function of the signal to noise ratio. This graph is equally valid for x- and y-positions and makes it possible to determine the maximum signal to noise ratio necessary for a certain accuracy. For example if a position accuracy of 0.01 mm is needed the signal to noise ratio has to be at least 35 dB ($\frac{A_{signal}}{A_{noise}} = 3162$). Of course this consideration is not the only error on the amplitude ratios, but it describes the effect of the noise on the detector's accuracy. The error of the calibration curve has been neglected in this calculation.

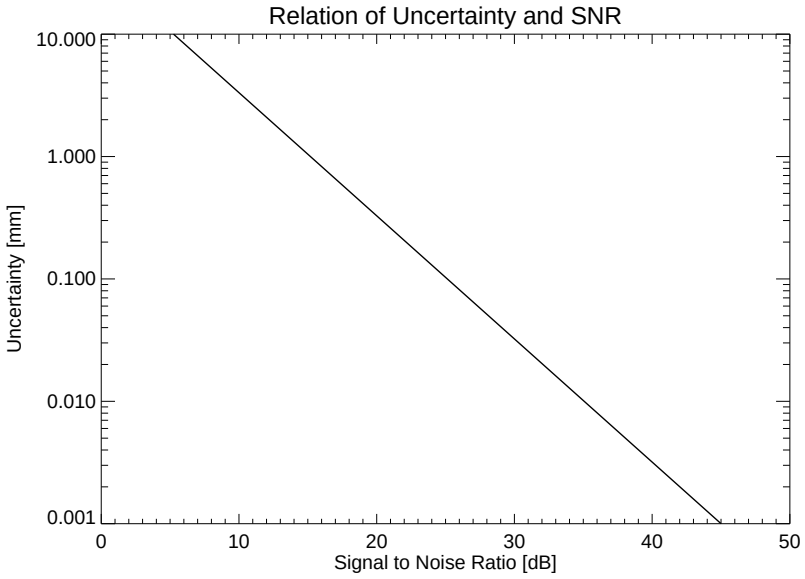

Figure 4.6: Maximum detector uncertainty as a function of the signal to noise ratio. Note the logarithmic scale.

The typical noise level on the detector signal is given by (1.11±0.41) fC. With a representative particle charge of 100 fC this results in a signal to noise ratio of approximately 20 dB ($\frac{A_{signal}}{A_{noise}} = 100$) and thus to a detector accuracy of about 0.3 mm. But this estimate has to be treated with caution as it is only based on uncertainty due to the effect of noise.
These calculations do not contradict the observations made in Fig. 4.2. There it can be seen that for larger displacements from the centre the amplitude ratio becomes more inaccurate. A more inaccurate ratio does not result in a larger position inaccuracy though. At higher amplitude ratios the position becomes less sensitive to amplitude ratio variations.

4.1.6 Detection Limit

The detector plates are shielded by copper panels and cylinders. Thus not all of the electric field lines end on the detector plates but some are lost to the shield-

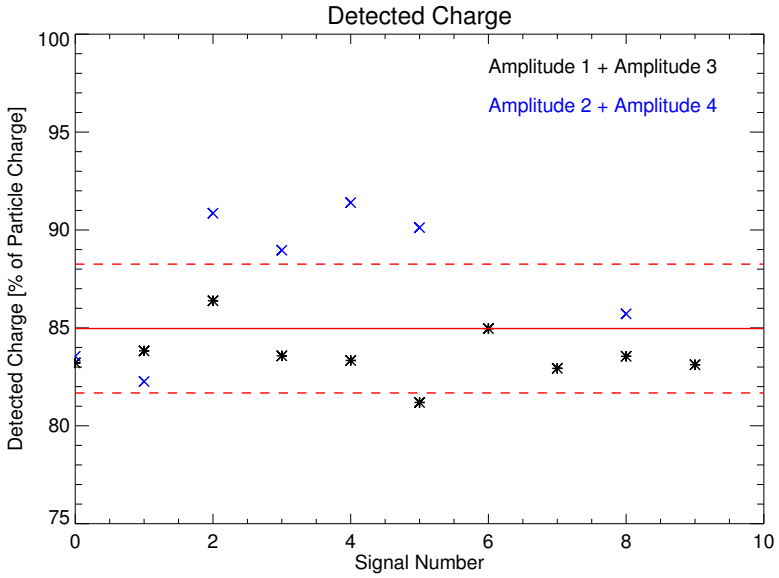

Figure 4.7: Percentage of particle charge detected by the position sensitive detector derived from A_1 and A_3 (black) and A_2 and A_4 (blue). The red solid line indicates the mean value and the red dashed lines its deviation. The percentage of the detected charge is (85.0±3.2) %.

ing. Thus fewer charge is induced on the plates. This section concerns the loss of induced charge and the resulting charge detection limit.
In order to determine the fraction of the particle charge that is detected by the position sensitive detector, a reference charge detector as described in Section 2.2.5 recorded ten signals due to dust passing through the centre of the detector. With this information the charge detected by the position sensitive detector could be correlated with the charge of the passing dust particle. Figure 4.7 shows the detected charge on the plates derived from A_1 and A_3 and the charge derived from A_2 and A_4. They should be equal if the particle charge was detected equally.

The position sensitive detector detects about (85.0±3.2) % of the charge that the dust particle carries. In addition, Fig. 4.7 shows that the charge detected by the plates which produce A_2 and A_4 (horizontal displacement) is about 3 % larger than the charge detected by the plates which produce A_1 and A_3 (vertical

displacement). This might be due to a slightly asymmetrical detector set up or installation in the beam line. Also the cables connecting the plates to the charge amplifier do not have the same length and thus different capacitances. This also has an effect on the charge amplification of different plates. The calculated arithmetic mean value did not distinguish between the different amplitude sums but was taken over all data points as the difference between the two amplitude sums can be neglected for the when estimating charge detection. Nevertheless, the plot gives an idea of the charge detection efficiency.
The absolute noise determined from the signals used in Fig. 4.7 to (1.11±0.41) fC. The detection limit DL_{cen} of the position sensitive detector is given by three times the standard deviation of the noise leading to $DL_{cen} = 3{\times}0.41$ fC = 1.23 fC for a particle passing through the centre of the detector. According to the calibration curves in Fig. 4.3 the maximum amplitude ratio is given by approximately 4. Thus if the smaller amplitude is three times larger than the standard deviation of the noise level the amplitudes sum to $15{\times}1.23$ fC = 18.45 fC. This means that the minimum charge DL_{off} a dust particle has to carry in order to be detected at any possible position in the beam line has to be $DL_{off} = 18.45$ fC.

4.2 Simulation Results

This section describes the simulation results of the position sensitive detector as calculated with the software package COULOMB [2011]. The simulation was used to plot signals, calculate an idealised calibration curve and determine the loss of induced charge for different trajectories through the detector. With this information the quality of the detector can be further investigated.
The simulations were provided by Jianfeng Xie and Dr. Zoltan Sternovsky from the Laboratory of Atmospheric and Space Physics at the University of Colorado at Boulder.

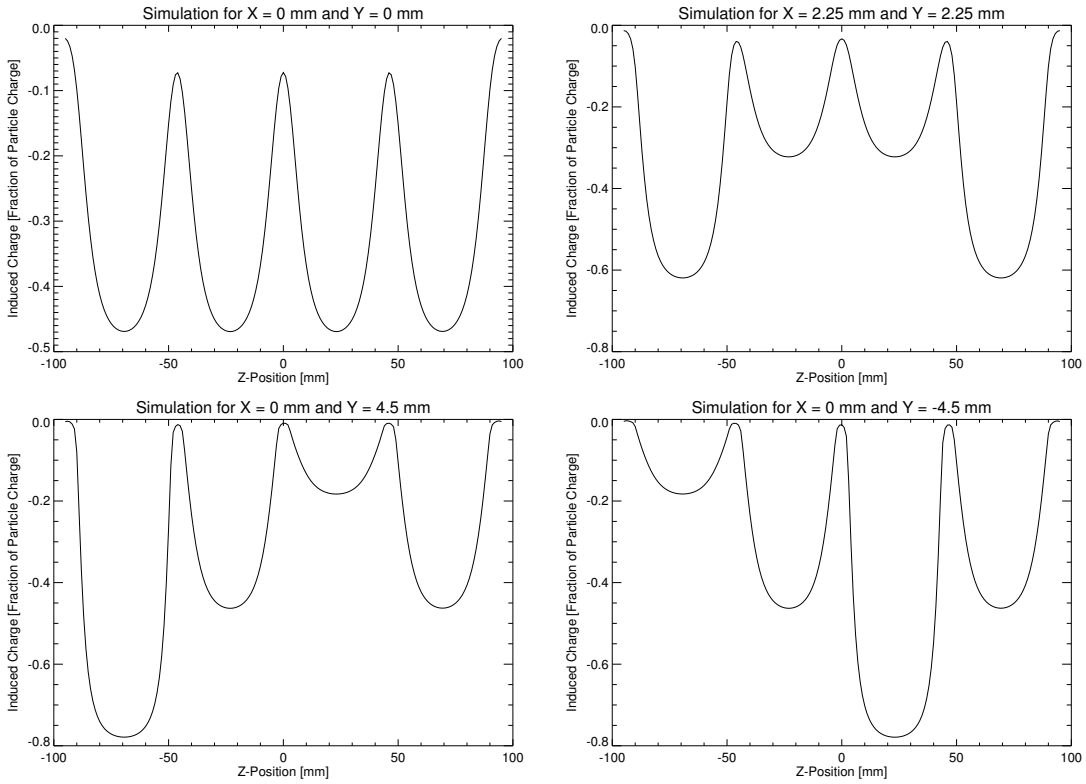

Figure 4.8: Example signals for different trajectories through the detector.

4.2.1 Simulated Signals

To simulate a detector signal the induced charge of the four detector plates that are connected to the charge amplifier in the real detector set up have to be added. Figure 4.8 shows resulting detector signals for a dust particle passing through the centre, x = -2.25 mm and y = 0 mm, x = 2.25 mm and y = 0 mm and at x = 4.5 mm and y = 4.5 mm. Note that the abscissae are given in millimetres and not time as in the real detector. This means that the simulation is valid for all particle speeds. The z position in the detector can easily be converted into time t when the speed v of the particle is known. It is given by $t = \frac{z}{v}$. The centre of the detector is set at z = 0 mm. The ordinates give the induced charge as fraction of the particle charge $Q_{particle}$ (set to $Q_{particle} = 1$ for these simulations). Note that the induced charge signal is negative as the particle is positively charged.

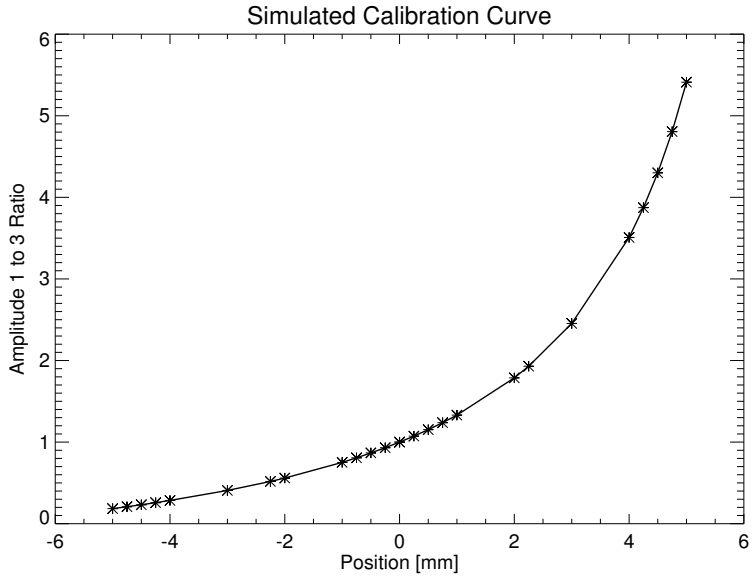

Figure 4.9: Simulated calibration curve.

The example signals in Fig. 4.8 also show that the further the particle trajectory is displaced from the centre the higher the signal rises between two plate troughs. For instance, the signal that passes the detector through the centre gives an induced charge rise to about -0.07 of the particle's charge while the signal for a trajectory with a displacement of 4.5 mm from the centre rises to zero induced charge. The closer a particle passes the panel's walls the more charge is "collected" by the panel. This leads to a further rise in the signal, as described in Section 4.1.1. The simulations for large displacements also show that the distance between two troughs is as wide as the copper panels width (5 mm).

4.2.2 Simulated Calibration Curve

In order to generate a calibration curve with the simulated signals the four amplitudes of each simulated signal (Q_1, Q_6, Q_4, Q_7) (corresponding to A_1,A_2, A_3, A_4 in the real detector) were determined. The ratios of Q_1 and Q_6 (corresponding to A_1 and A_3) were calculated and plotted against the y-position of their simu-

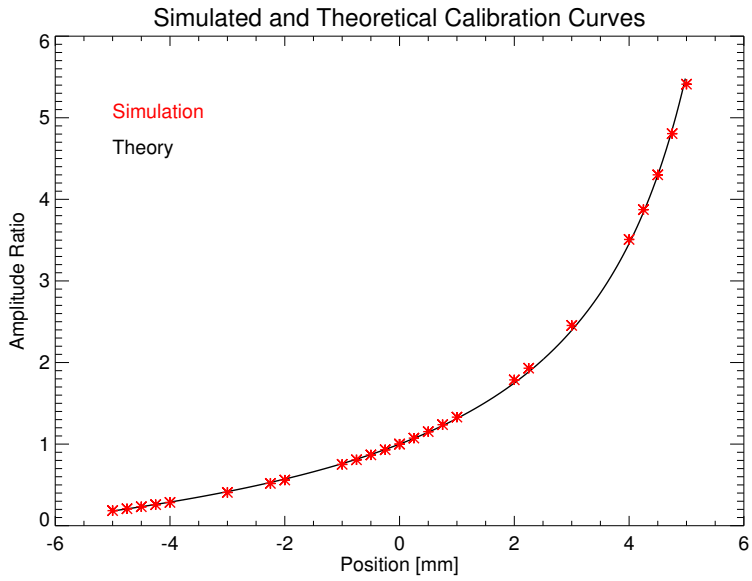

Figure 4.10: Simulated and theoretical calibration curves.

lated trajectory and the ratios of Q_4 and Q_7 (corresponding to A_2 and A_4) were plotted against the x-position of their simulated trajectory. As the simulation is idealized the two calibration curves are the same for the x- and y-position. Figure 4.9 shows the result.

Owing to the simulated trajectories (Table 3.2) there are more than one data point for the positions at y = 0 mm, y = 2.25 mm and y = 4.5 mm. These were considered when calculating the calibration curve but cannot be distinguished in it as they are much too close to the other data points with the same y value.

Figure 4.10 shows the simulated and theoretical calibration curves calculated with the theory explained in Section 2.2.2. For the theoretical curve a plate size as large as the plate size in the simulation and an image charge number of 100 was used. The two curves almost match each other. This means that the simulated detector is nearly as precise as the theory allows. The slight offset is due to the shielding panels and cylinder considered in the simulation that cause charge loss on the detecting plates.

The simulated calibration curve thus describes the real detector set up adequate and makes it possible to calculate idealised detector signals. The difference in

comparison with the real detector signals is explained by loss of induced charge due to further shielding and inaccuracies due to noise and manual amplitude reading that have been neglected in the simulation.

4.2.3 Charge Loss

Figure 4.10 shows that the simulated calibration curve varies slightly from the theoretical curve. The simulation considers shielding panels and cylinders that are neglected in the theory. This section explains how much the shielding effects the charge that is induced on the simulated plates. The corresponding charge loss is calculated for different particle trajectories.

To examine this loss of induced charge the sum of Q_1 and Q_6 (corresponding to A_1 and A_3 in the real detector) and Q_4 and Q_7 (corresponding A_2 and A_4) were calculated. For designation of the charge signals see Fig. 3.2. The sums were then subtracted from the particle charge $Q_{particle} = 1$ for each simulated detector signal.

Figures 4.11 and 4.12 show the result. The right picture indicates where the trajectories are located between the two plates. The x-y-plane is identical to the paper plane and the particle trajectory is perpendicular to it. Thus the dashed lines do not indicate one particle trajectory but the location of all simulated particle trajectories. The left picture shows the charge loss for the indicated trajectories. A square function was used to approximate the curve between the data points.

The charge amplitudes of the horizontal plates (y-detecting plates) were considered for different x- and y-positions of the particle trajectory. Figure 4.11 shows the charge loss for three different y-positions (y = 0 mm, y = 2.25 mm and y = 4.5 mm). Figure 4.12 shows the charge loss perpendicular to the detecting plates for three different x-positions (x = 0 mm, x = 2.25 mm and x = 4.5 mm).

Consider trajectories along the z-axis with a fixed y-position and variable x-positions (Fig. 4.11). When detecting charge on the horizontal plates the minimum charge loss for these trajectories is in the centre between the plates. This is

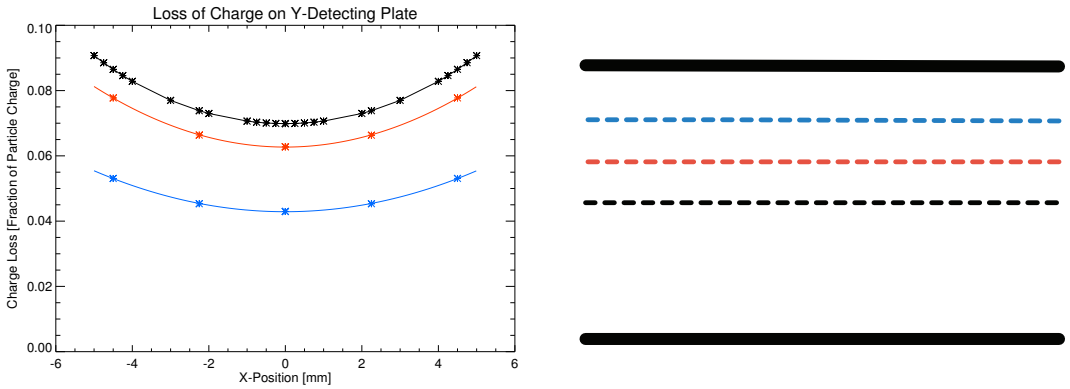

Figure 4.11: Charge loss for a set of particle trajectories parallel to the detecting plate pair (left) and sketch of trajectory sets (right). Black symbolises trajectories with y = 0 mm, red trajectories with y = 2.25 mm and blue trajectories with y = 4.5 mm.

due to more electric field lines ending on the detecting plates than for positions closer to the edge of the plates. Thus fewer charge is induced on the shielding and more charge is induced on the plates. With larger approaches to one of the detecting plates (red and blue dashed lines in Fig. 4.11) the charge loss becomes less. This is due as a detecting plate "intercepts" more induced charge the closer the charge is.

Now, consider trajectories with a fixed x-position and variable y-positions (Fig. 4.12). When detecting the charge on the horizontal plates a larger charge loss occurs in the centre between the two plates. The further the particle trajectories approach one of the detecting plates the more field lines end on that plate and fewer are lost to the shielding. For particle trajectories further to the edge of the detecting plates (red and blue dashed lines in Fig. 4.12) the charge loss becomes larger as more induced charge is now lost to the shielding.

In general the charge loss does not exceed 9.1 % of the particle charge and does not fall below 3.7 %. The consideration does not explain how the charge loss is distributed between the two detecting plates though. Assuming that the charge loss is equally distributed between the two plates this only would yield no amplitude ratio difference for particles in the centre (amplitude ratio = 1). Particles

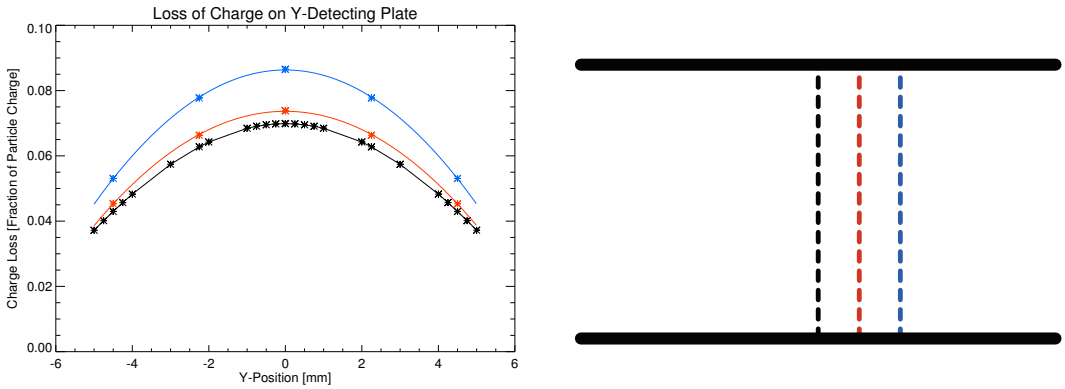

Figure 4.12: Charge loss for a set of particle trajectories perpendicular to the detecting plate pair (left) and sketch of trajectory sets (right). Black symbolises trajectories with x = 0 mm, red trajectories with x = 2.25 mm and blue trajectories with x = 4.5 mm.

with a displacement from the centre would show a deviation in the amplitude ratio. Also, for these particles the charge loss might not be equally distributed between the two detecting plates. Unfortunately, this cannot be read off by the given simulation.

5 Discussion and Summary

5.1 Comparison of Experiment and Simulation

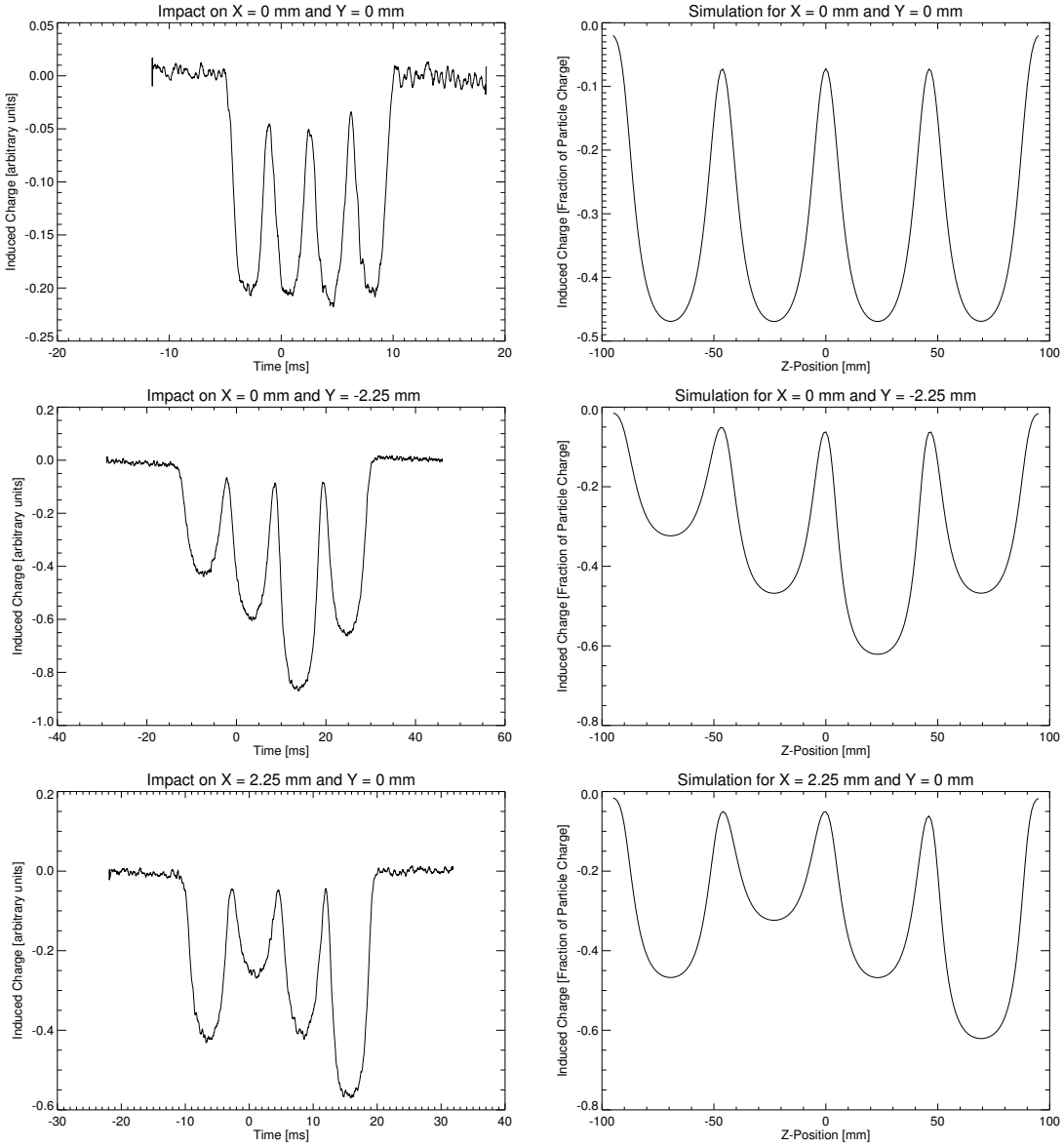

Figure 5.1: Measured and simulated signals for particle trajectories at positions x = 0 mm, y = 0 mm and x = 0 mm, y = 2.25 mm and x = 2.25 mm, y = 0 mm.

The simulation was calculated to support the experimental results and help ascertain the detector accuracy. This section discusses and compares the simulated and experimental results.

Figure 5.1 shows the recorded signals and their simulated equivalents for three different particle positions. Even though the speed of the recorded signals varies, which makes a signal broader or more narrow, the amplitude ratios are well represented by the simulated signals. As only the amplitudes provide information about the position of the particle in the detector, the simulated and recorded signals give the same conclusion about the particle's position. Of course the signals' amplitudes vary slightly from each other as the position of the impact in the detector could only be determined to an accuracy of 1 mm in the x- and y-directions.

The charge induced on the detector plates while the particle passes through the copper apertures is dependent on the position of the dust particle in the detector as described in Section 4.1.1. The effect can be seen in both, the recorded and simulated signals. The peaks of the signal between two amplitudes is greater the closer the dust particle passes to the aperture's wall. This shows the effect of the panels on the signal but does not have any influence on the amplitude measurement which is needed for the determination of the position. Nevertheless, it seems that the shielding by the panels is more efficient for larger displacement from the centre of the beam line.

Using the numerical simulations and the theory concerning a charge between two conductive plates, as described in Section 2.2.2, the idealised calibration curves could be determined. They give an idea of the calibration curve's run. All three calibration curves are plotted in Fig. 5.2. The experimental calibration curve for vertical displacement was only used as both experimental calibration curves have the same slope shape. Also, the horizontal displacement calibration curve shows an offset of -0.2 that is neglected in the following considerations as it does not change the slope shape of the curve itself. This might be due to asymmetric charge induction in the detector (Section 4.1.3).

As described in Section 4.2.2 the theoretical and simulated calibration curves al-

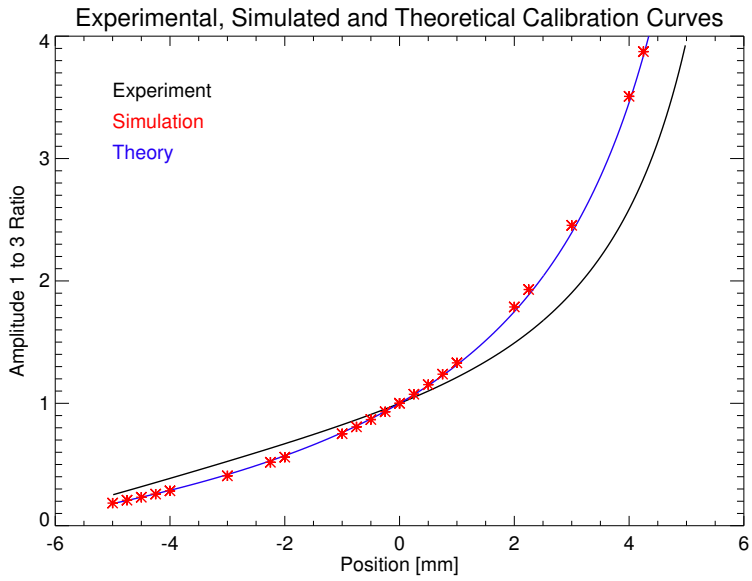

Figure 5.2: Measured (black), simulated (red) and theoretical (blue) calibration curves.

most match each other. This means that the simulation gets nearly as precise as the theory, even though the simulation considers the panels and shielding.
However, the experimental calibration curve is shallower than the idealised curves. That is fewer charge is induced on the plate that produces the larger amplitude than in the idealised detector. This might be due to the loss of induced charge to the screening and panels in the real detector.
The shallower calibration curve was fitted by assuming the size of the detecting plates to be half the size they actually are in the existing detector. This is adequate to compensate the occurring charge loss. Thus the difference of the simulated and experimental curves can be explained by a reduction in the effective detecting plate size in the existing detector without knowing further detail about the distribution of charge loss to shielding and panels.
In Section 4.1.6 and Section 4.2.3 the charge loss of the actual and simulated detector was determined. The existing detector is able to detect (85.0±3.2) % of the particle charge while the charge loss of the simulated detector does not exceed 9.1 %. Thus the simulated assembly detects about 5.9 % more charge

than the actual detector. This is a good agreement as the simulated detector neglects charge loss due to further shielding and cable capacitances that occur in the real assembly.

5.2 Comparison with Other Position Detector Designs

The Heidelberg Dust Accelerator previously utilised different detectors to determine the charge and position of a dust particle in the beam line (Section 2.2.5). This section places the results of the new position sensitive detector in context with the previously developed and installed detectors.

The low charge detector as described by Srama and Auer [2008] can be used to determine the charge of a dust particle. Even though it is assembled with the same model Amptek charge amplifier as the position sensitive detector, it has a much lower noise level of 0.15 fC (compared to 1.1 fC) under operational conditions. Thus the position sensitive detector is less sensitive at charge detection. Its charge detection limit was determined to be 1.23 fC while the low charge detector is capable of detecting 0.2 fC. This is due to the different detector designs. As the low charge detector was designed to measure charges it employs a conductive cylinder to detect the charge with only little induced charge loss. The plates of the new position detector are more sensitive to charge loss to the shielding and thus the noise becomes more prominent.

The wire position detector as described by Srama [2005] was previously developed to determine the position of a particle in the beam line. The new position sensitive detector is more sensitive and potentially more accurate in position determining than the wire position detector. As it uses conductive plates instead of wires more charge can be detected. The new position sensitive detector detects 85 % of the particle charge while the wire detector only detects 32 %. Thus the charge detection limit of the plate position detector is, at 1.23 fC, more than eight times lower than the detection limit of the wire detector (10 fC). Unfortunately, as the wire position detector has not yet been calibrated the accuracy of both detectors cannot be compared at this point.

Even though the new position sensitive detector has a higher charge detection threshold than the low charge detector, it is still an improvement in charge detection to the former position detector. Also, the signals of the new position sensitive detector can be mapped to the location of a particle in the detector with the calibration curves determined in this work.

5.3 Summary

A position sensitive detector based on charge induction was calibrated and analysed via experiments and simulations in this thesis.
The detector uses four pairs of parallel electrode plates in which one plate is grounded and the opposite one connected to common charge amplifier. The plate pairs are shielded from each other by copper panels. This results in a detector signal with four amplitudes, one for each plate pair. A passing charged dust particle induces charge on each electrode depending on the position of the particle between the two plates. The ratio of the induced charge on two opposing electrodes yields the position of the particle in the direction perpendicular to the plate pair without the need to determine the total particle charge.
The position sensitive detector was implemented in the beam line of the Heidelberg Dust Accelerator and successfully tested. Detector signals were recorded for particles with various speeds, charges and positions in the beam line. The amplitude ratios of the opposing electrode plates were determined by a self-developed IDL-based software programme which used the Canny edge detection algorithm [Canny, 1986].
A calibration set up utilising a segmented target plate as an independent position measurement was developed and implemented in the beam line. The target was coated with 1 mm^2 electrode segments that were connected to separate charge amplifiers to determine the impact charge on each segment. A second self-developed IDL-based software programme using the Canny edge detection algorithm [Canny, 1986], was written to measure the charge rise. The impact location could be ascertained for five different horizontal and vertical particle po-

sitions. The position was mapped to the detector signals resulting in a calibration curve for each direction.

The experimental calibration curves for horizontal and vertical displacement from the centre of the detector were established by using the ratio of the signal amplitudes and found to only differ by an offset of -0.2 but not in the curve slope showing a high symmetry in the detector set up. Furthermore the accuracy of the detector due to the signal to noise ratio of the recorded signals were calculated and a relation between the signal to noise ratio and detector accuracy were established. About (85.0 ± 3.2) % of the particle charge is induced on the position detecting plates. With an average noise level on the detector signals of (1.11 ± 0.41) fC this leads to a general charge detection limit of 18.45 fC. For particles passing through the centre of the detector this this limit is reduced to 1.23 fC.

In cooperation with the Laboratory of Atmospheric and Space Physics at the University of Colorado at Boulder the existing assembly was simulated using the software programme Coulomb [2011]. The simulation was used to calculate detector signals for certain particle positions considering the detector's shielding panels and the inner shielding cylinder. A calibration curve was produced that matches the theoretical calibration curve for a charge between two finite conductive plates. Additionally, the induced charge loss depending on the particle position was determined and found to be between 3.7 % and 9.1 % of the particle charge.

The experiments and simulations show good agreement. The signal shapes match well, but the calibration curves differ slightly due to induced charge loss in the experimental set up. The simulated amplitude ratios show a steeper relation with distance from the centre of the detector than the experimental ratios. The effective detecting plate size in the existing position sensitive detector was determined to be half of the plate size that is actually used.

All things considered the position sensitive detector installed in the dust accelerator's beam line is a valuable and reliable device for determining a dust particle's trajectory.

6 Outlook

6.1 Improvement to the Position Detector Assembly

The position sensitive detector performs well in mapping a detector signal to a particle position in the beam line. Nevertheless, adjustments to the assembly that could help to improve the detector's performance are described in this section.
The experimental calibration curves in Section 4.1.3 show that the theoretical fit that matches the data best uses a detector plate size that is half as big as the detector plates in the assembly. Additionally, Section 4.1.6 shows that about 15 % of a dust particle's charge is lost due to the shielding and the limited plate size. This limits the precision of the position derived from the detector's signals. In order to detect the charge more efficiently the detector assembly has to be more sensitive to charge induction. This can be achieved by extending the detecting plate size and reducing the plate separation distance.
Extending the plate size is difficult as the detector is placed inside a copper cylinder of fixed radius. Also a bigger plate size is more sensitive to disturbance. Thus reducing the plate distance is a more suitable way to improve the detector performance. The present position detector uses a plate distance of 15 mm. As the particle trajectories are limited by the 10 mm round orifice in the shielding panels the distance of the plates can be reduced to almost 10 mm. By reducing the plate distance, more charge will be induced on each plate as the induced surface charge σ increases with decreasing distance r ($\sigma \propto \frac{1}{r^2}$), see Eq. 2.22.
Figure 6.1 shows the calibration curve of the position sensitive detector described in this thesis and the theoretical calibration curve calculated using a plate distance of only 11 mm instead of 15 mm. The same plate size was assumed for both curves. The gradient of the amplitude ratio in the improved assembly is larger than in the calibration curve of the present detector. This makes it more precise in determining a particle's position, but for low charged dust grains the position with large displacement from the detector's centre raises another difficulty. A large amplitude ratio implies that one amplitude has to be small compared to the other. But the smaller amplitude still has to be larger than the noise. This

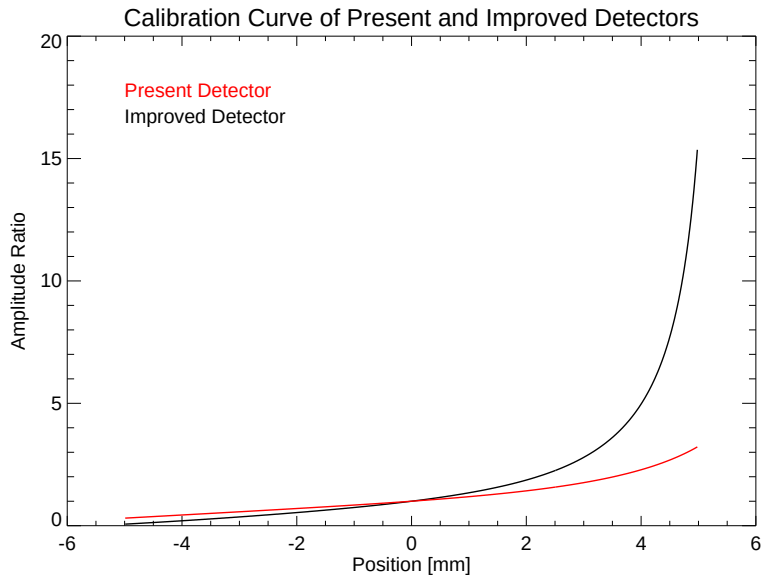

Figure 6.1: Calibration curve of the present detector (red) and theoretical improvement of the calibration curve (black) using a plate distance of 11 mm.

is partly compensated for by the presumably larger induced charge on the plate pairs as the electric induction is more effective for smaller plate distances. Thus the amplitude ratios would yield a more precise particle position in the improved position detector assembly for suitable charged dust particles.
An adjustment to the present simulation would provide a better understanding of the detector's performance with smaller plate distances.

6.2 Calibration Using Light Amplifier

For an accurate calibration that maps the detector signal to the position of a dust particle in the beam line, the absolute particle position in the horizontal and vertical directions has to be better constrained. One possibility producing a more precise calibration curve is given by performing an experiment using a quartz target and a light amplifier.
A high velocity dust grain impacting on a quartz plate produces a light flash

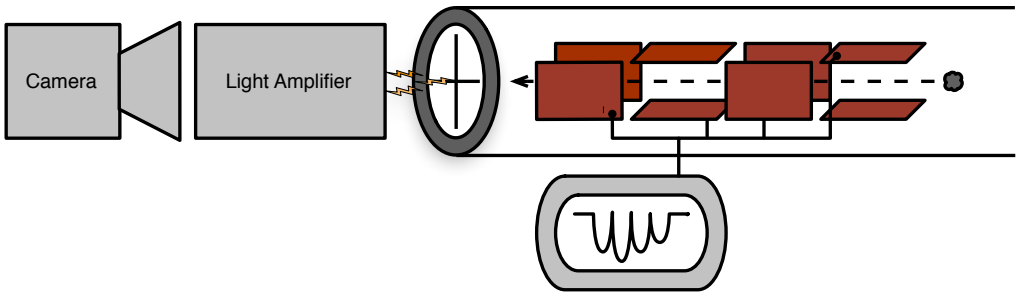

Figure 6.2: Sketch of calibration set up with light amplifier.

within the visual spectral range around 350 nm to 680 nm as described by Frichtenicht [1966] and Eichhorn [1975]. By using a light amplifier with a high spatial resolution a particle impact can be mapped to a position in the beam line. Figure 6.2 shows the sketch of a possible set up for this calibration. After a particle passes the position detector it hits a quartz target with a reference scale and produces a light flash. Ideally the quartz target is the window of the vacuum beam line. Outside the beam line a light amplifier and camera record the impact light flash. With the help of the reference scale on the target the absolute position of the impact and thus the particle's trajectory can be determined and mapped to the position detector's signal.

This set up would make the reference position determination for the position detector more precise and thus the calibration curve more reliable. It would also provide the possibility of calibrate using every possible position in the beam line. A possible inaccuracy might occur from diffraction and scattering of the light flash by passing through the beam line window and amplification process. Also the spatial determination of the particle impact is limited by the light flash expansion.

Nevertheless this set up can lead to a more detailed and substantiated calibration curve.

A Evaluation Software

A.1 Detector Signal Analysis

This section describes the IDL programme called GUI that was written to evaluate detector signals from the position detector in the dust accelerator's beam line. The detector signals show four amplitudes of induced charge on a metal plate that give information about the particle position. The programme shifts and smooths the signals. It finds the signal's edges, its four amplitudes and the signal to noise ratio of each interval separated by edges and stores these values.
To open data files click OPEN FILES. The window allows to pick multiple files by holding the mouse button while choosing the files. Navigate to the desired files and click OK. Once you clicked OK a SAVING PROPERTIES window appears and asks you to name the variable in which the evaluated data will be saved later. After clicking OK in this window the evaluating process will start.
The window will show a detector signal. If the signal shall be evaluated click OK, otherwise click the next arrow until you find an adequate signal. Click OK before proceeding with the evaluation process, see step 1 in Fig. A.1.
Once OK was clicked the range in which the four amplitudes lie has to be specified by pressing the left mouse button to designate the beginning of the range followed by the right mouse button to designate its end. Choose the smaller limit with the left mouse button first followed by the higher limit with the right mouse button. The program will lead to an error if the order is switched and will not continue until the right mouse button has been pressed.
Next a new plot appears with the signal in the selected range. A base line has to be drawn in the plot by again clicking the left mouse button first for the beginning of the line and the right one for the end of the line, see step 2 in Fig. A.2. The base line occurs in the plot and a new plot with the shifted and smoothed signal appears. If satisfied with the signal processing click START ANALYSIS; click RESET to redo the work on this signal. RESET can be clicked at any time during the process, see step 3 in figure A.3.
Please allow the program some time to evaluate the signal after clicking START

ANALYSIS. In order to ascertain the amplitudes the signal's edges were determined by the Canny edge algorithm. It allows to detect an edge by applying a filter based on the first derivative of a Gaussian that neglects edges due to noise [Canny, 1986]. After running the Canny edge algorithm on the signal the same signal appears on the screen with vertical lines drawn where the algorithm found edges and horizontal lines that indicate the median value of the data points between the edges. The horizontal lines are supposed to line up with the four amplitudes, see step 4 in figure A.4.

For a general correction of the amplitude levels click on CORRECT PLATEAU: LOWER or CORRECT PLATEAU: HIGHER. To correct the horizontal lines that indicate the amplitudes separately and save them click SAVE. Note that once SAVE has been clicked the RESET button can not be used any more. Use the left mouse button to click on the four amplitudes in the specified ranges between the vertical lines. After clicking inside the plot four times a notification which values have been saved will appear in a little window, see step 5 in Fig. A.5. Click on OK and go on with the next signal by clicking the next arrow.

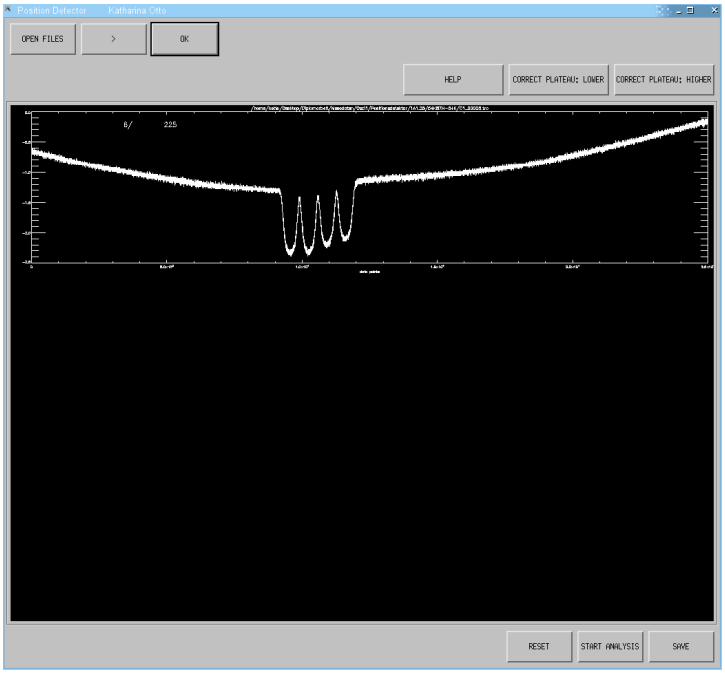

Figure A.1: Step 1 of the software written to analyse a position detector's signal.

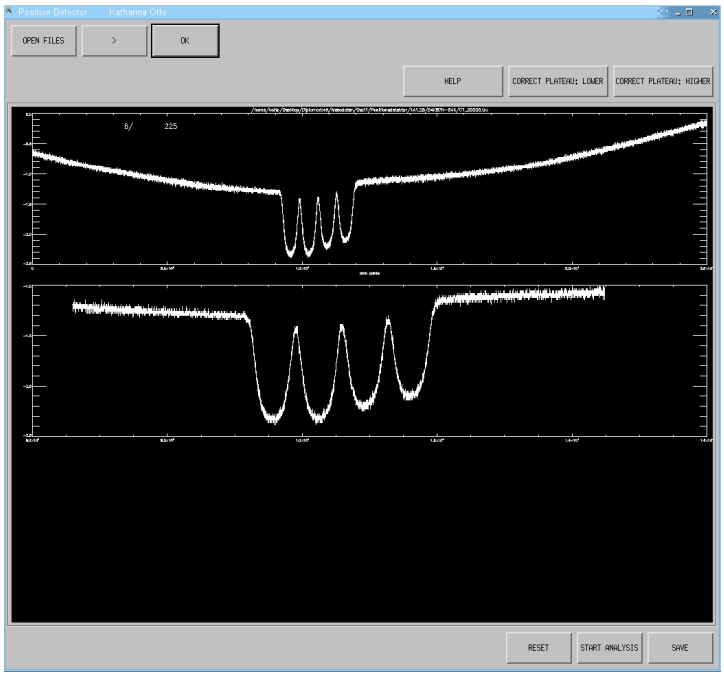

Figure A.2: Step 2 of the software written to analyse a position detector's signal.

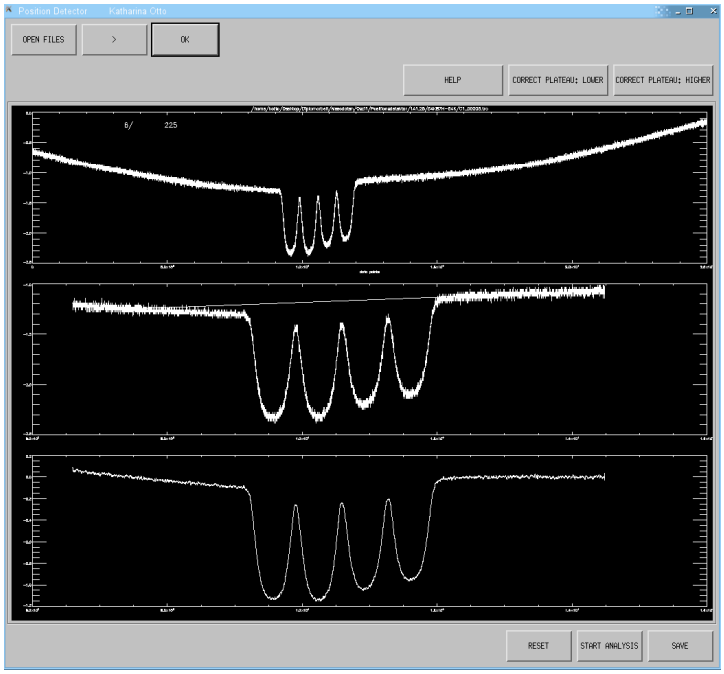

Figure A.3: Step 3 of the software written to analyse a position detector's signal.

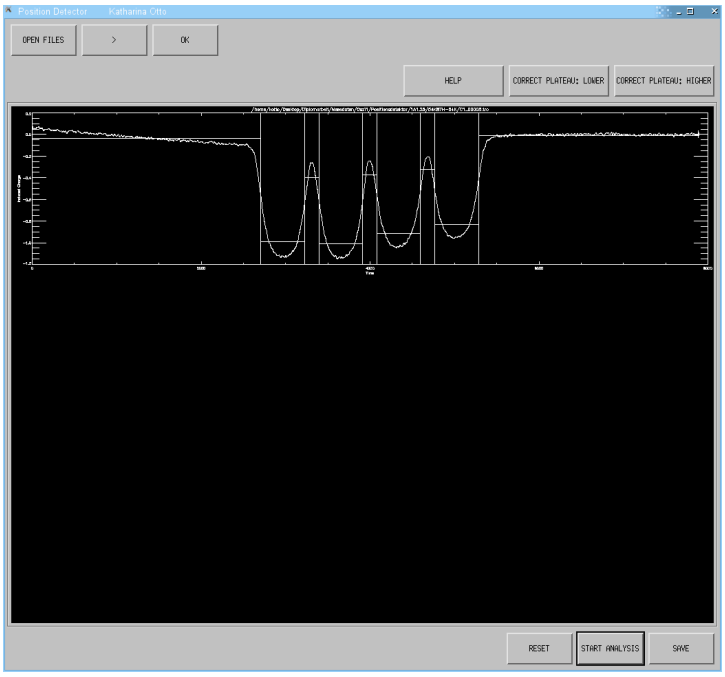

Figure A.4: Step 4 of the software written to analyse a position detector's signal.

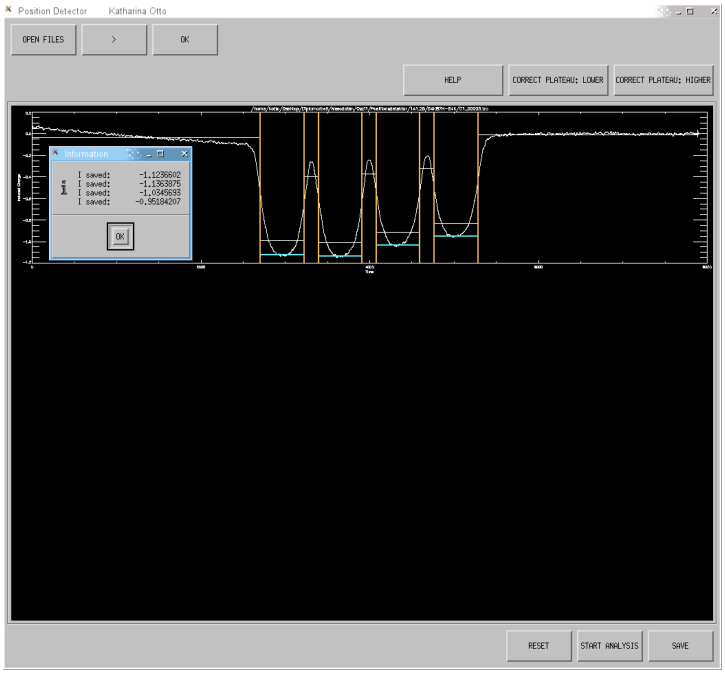

Figure A.5: Step 5 of the software written to analyse a position detector's signal.

A.2 Impact Signal Analysis

This section describes the evaluation software called IMPACT_GUI that was written to evaluate the charge response of all attached charge amplifiers after a dust particle impacted on the segmented target behind the position sensitive detector. It saves the time of each of the impact signals, the upper and lower charge level and the charge respond that is given by the difference of these two values. Additionally the noise and evaluation status is saved.

After starting the programme a SAVING PROPERTIES window appears in order to name the variable in which the evaluated data will be saved later. After clicking OK in this window the evaluating process will start.

The programme window has has five buttons on the top and shows the detector and set of impact signals in eight plots below them. The position detector signal is shown twice, once for each oscilloscope the impact signals were recorded on to make sure they show the same impact event. Use the NEXT and PREV buttons to switch between the impact events. In the top left plot the event number out of the total amount of events is shown, see step 1 in Fig. A.6.

Once a signal was chosen to be evaluated click on ANALYSIS to start the algorithm that finds the edges in the shown set of impact signal. For this purpose the Canny edge detection algorithm was used [Canny, 1986]. Three lines will occur in each impact signal plot. One green vertical line that indicates the impact time and two purple horizontal lines that give the values short before and after the impact time, see step 2 in Fig. A.7.

A right mouse click in one of the impact signal's plots opens a menu to adjust the vertical lines in it if necessary, see step 3 in Fig. A.8. By choosing DEFINE UPPER LINE or DEFINE LOWER LINE the lines will be erased temporarily and a single white line appears that now can be adjusted to the signal manually, see step 4 in Fig. A.9.

When all impact signals' levels are correct click on SAVE. A window will open that indicates that the signal was stored. Click on OK to continue the evaluation process with the next impact event, see step 5 in Fig. A.10.

During the whole evaluation process the button EINDEUTIG can be clicked to

mark the set of impact signals. This is useful to sort out explicit signals out of the impact events later on but does not have to be used.

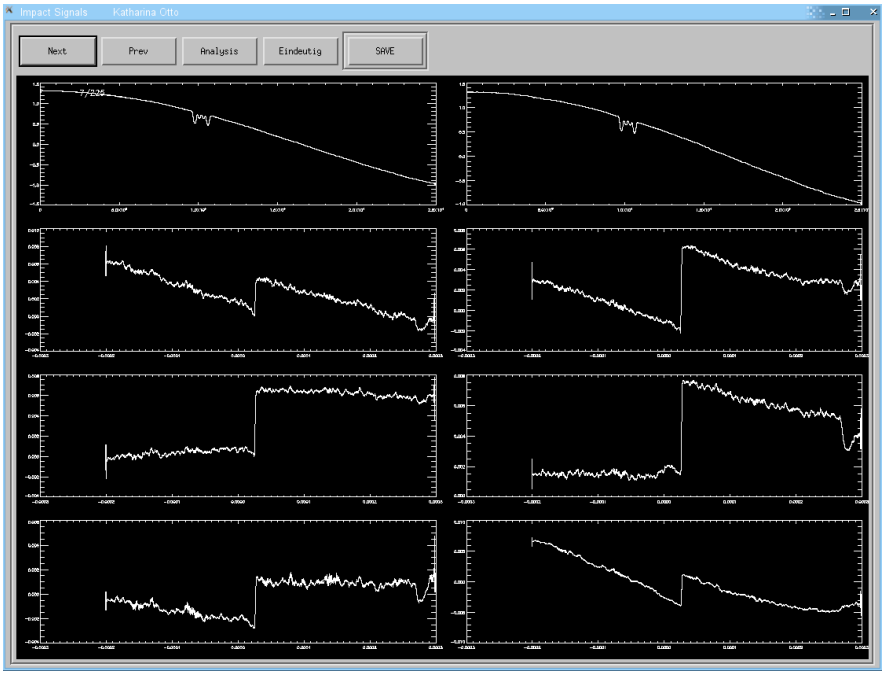

Figure A.6: Step 1 of the software written to analyse dust impact signals.

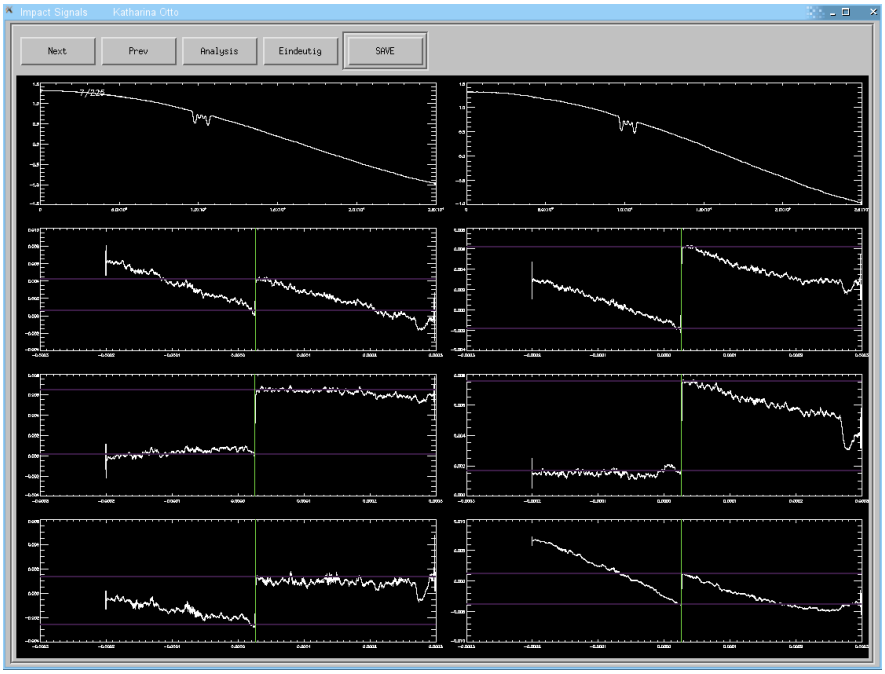

Figure A.7: Step 2 of the software written to analyse dust impact signals.

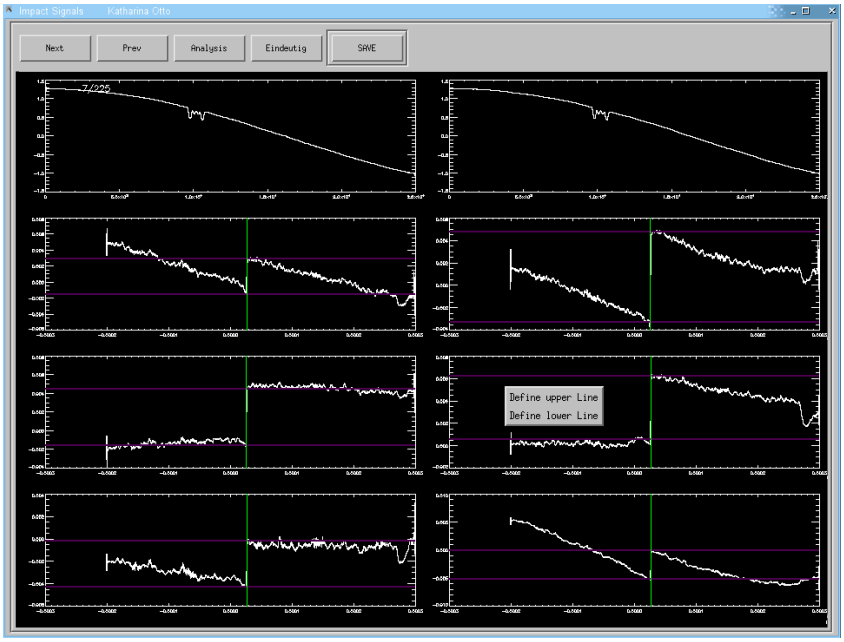

Figure A.8: Step 3 of the software written to analyse dust impact signals.

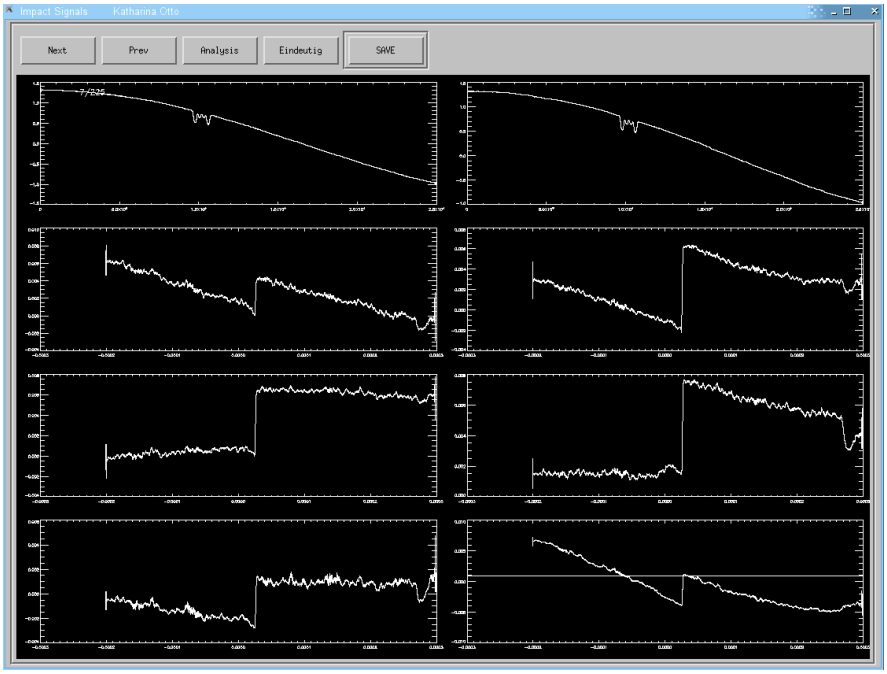

Figure A.9: Step 4 of the software written to analyse dust impact signals.

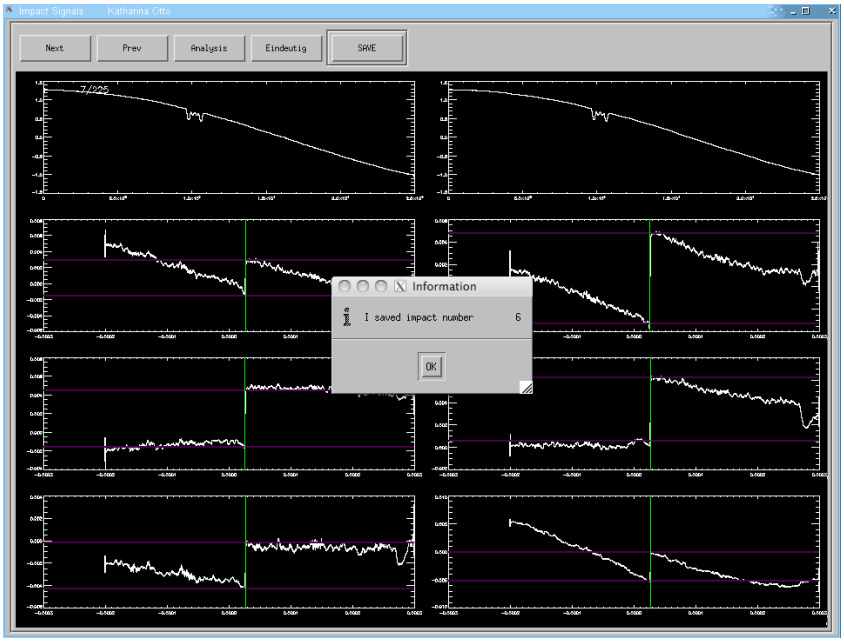

Figure A.10: Step 5 of the software written to analyse dust impact signals.

B Software Code

To evaluate the detector signals and determine the impact of a dust particle on a target segment computational methods were needed. The evaluation code was written in IDL language. This chapter gives an overview of the most important functions written for this purpose.

B.1 Image Charge

The following code calculates the ratio `ratio` of the induced charge on two conductive plates when a charge is located between them. It takes five parameters: the position of the charge between two plates `x`, the charge `Q`, the distance of the plates `d`, the number of image charges to consider `N` and the plate size `R`.

```
FUNCTION imageCharge , x, q, d, N, R
   qnR = fltarr(N+1)
   qnL = fltarr(N+1)
   sumR = fltarr(n_elements(x))
   sumL = fltarr(n_elements(x))
   FOR m=0, n_elements(x)-1 DO BEGIN
      qnR[0] = q
      qnL[0] = q
      FOR i=1, N DO BEGIN
         zR = (2*i-1)*d/2+x[m]*(-1)^i
         zL = (2*i-1)*d/2-x[m]*(-1)^i
         qnR[i] = -qnL[i-1]*(1-(zR)/sqrt(R^2+zR^2))
         qnL[i] = -qnR[i-1]*(1-(zL)/sqrt(R^2+zL^2))
      ENDFOR
      sumR[m]=total(qnR)
      sumL[m]=total(qnL)
   ENDFOR
   ratio = sumL/sumR
```

```
   RETURN, ratio
END
```

B.2 Target Hit

The following code determines if which particles impacted on a certain target segment and returns their amplitude ratios `plo`. It takes four parameters: the impact information `impactinfo1`, the target number `target`, the limit of the impact signal difference `grosse` and the amplitude ratio `ratio`.

```
FUNCTION hit_target, impactinfo1, target, grosse, ratio
count=0
plo=0
print, 'target', target
IF target NE 0 AND target NE 5 THEN BEGIN
   FOR i = 0, n_elements(ratio)-1 DO BEGIN
      IF ratio[i] LT 1000 THEN BEGIN
         IF abs(impactinfo1[target,i] GT $
          max(abs([impactinfo1[0:target-1,i], $
           impactinfo1[target+1:5,i]]))*grosse) THEN BEGIN
            plo = [plo,ratio[i]]
            count++
            print, 'geplottetes Signal', i
         ENDIF
      ENDIF
   ENDFOR
ENDIF ELSE BEGIN
   IF target EQ 0 THEN BEGIN
      FOR i = 0,n_elements(ratio)-1 DO BEGIN
         IF ratio[i] LT 1000 THEN BEGIN
            IF abs(impactinfo1[0,i]) GT $
             max(abs(impactinfo1[1:5,i]))*grosse THEN BEGIN
```

```
               plo = [plo,ratio[i]]
               count++
               print, 'geplottetes Signal', i
            ENDIF
         ENDIF
      ENDFOR
   ENDIF ELSE BEGIN
      FOR i = 0, n_elements(ratio)-1 DO BEGIN
         IF ratio[i] LT 1000 THEN BEGIN
            IF abs(impactinfo1[5,i]) GT $
             max(abs(impactinfo1[0:4,i]))*grosse THEN BEGIN
               plo = [plo,ratio[i]]
               count++
               print, 'geplottetes Signal', i
            ENDIF
         ENDIF
      ENDFOR
   ENDELSE
ENDELSE
plo=plo[1:n_elements(plo)-1]
print, 'count:' + string(count)
RETURN, plo
END
```

B.3 Find Jump

The following code calculates the step of a jump `v`, the location of a jump `loc`, the upper line `up`, the lower line `low` and the noise level `noise`. It takes two parameters: The time vector `x1`, the signal vector `y1`.

```
FUNCTION find_jump, x1, y1, ampl, state
  radius = 50
```

```
radVec = [radius, 100]
sl=0.
noisevec = 0.
edge1 = analyseEdges(y1, radVec)
xx1=indgen(n_elements(x1))
flank = [0,edge1.minmaxidx,n_elements(x1)-1]
flank3 = cancel_entry(flank)
flank3 = cancel_entry(flank3)
FOR i=0, n_elements(flank3)-2 DO BEGIN
  a= flank3[i]
  b= flank3[i+1]
  yy1=y1[a:b]
  xxx1=xx1[a:b-1]
  IF n_elements(xxx1) GT 2*radius THEN BEGIN
    fitpar = linfit(xxx1[radius:n_elements(xxx1)-radius], $
     yy1[radius:n_elements(xxx1)-radius])
    m = fitpar[1]
    b = fitpar[0]
    yyy1 = yy1-(m*xxx1)
    dif = yy1 - (m*xxx1+b)
    noise = stddev(dif)
    noisevec = [noisevec,noise]
    sl=[sl,m*xxx1+b]
  ENDIF ELSE BEGIN
    fitpar = linfit(xxx1[0:n_elements(xxx1)-1], $
     yy1[0:n_elements(xxx1)-1])
    m = fitpar[1]
    b = fitpar[0]
    yyy1 = yy1-(m*xxx1)
    dif = yy1 - (m*xxx1+b)
    sl=[sl,m*xxx1+b]
```

```
    ENDELSE
ENDFOR
  sl=sl[1:n_elements(sl)-1]
  noisevec = noisevec[1:n_elements(noisevec)-1]
  diffvec=0
  fl= cancel_entry(cancel_entry(edge1.minmaxidx))
  FOR n=0, n_elements(fl)-1 DO BEGIN
    diff = abs(sl(fl[n]+5)-sl(fl[n]-5))
    diffvec = [diffvec,diff]
  ENDFOR
  diffvec= diffvec[1:n_elements(diffvec)-1]
  signoi = diffvec/noisevec
  jump = where(signoi EQ max(signoi))
  v = diffvec[jump]
  loc = x1[fl[jump]]
  up = sl[fl[jump]+5]
  low = sl[fl[jump]-5]
  noise = noisevec[jump]
  edgenjump = [v, loc, up, low, noise]
  RETURN, edgenjump
END
```

B.4 Uncertainty

The following code calculates the position uncertainty of the detector `delta` based on the calibration curve and signal to noise ratio. It takes five parameters: the normalized noise level `relerr`, the charge `Q`, the distance of the plates `d`, the number of image charges to consider `N` and the plate size `R`.

```
FUNCTION uncertainty, relerr, Q, d, N, R
par = [Q, d, N, R]
y = findgen(10000)/1000. - 5.
```

```
A1vsA3 = imageCharge(y,par)
invertfunc = fltarr(10000)
yw1 = fltarr(10000)
yw2 = fltarr(10000)
w1 = (A1vsA3+relerr*(A1vsA3+1))/(1-relerr*(A1vsA3+1))
w2 = (A1vsA3-relerr*(A1vsA3+1))/(1+relerr*(A1vsA3+1))
FOR a = 25, 9975 DO BEGIN
   invw1 = max(where(A1vsA3 LT w1[a]))+1
   invw2 = max(where(A1vsA3 LT w2[a]))+1
   IF invw1 LT n_elements(A1vsA3) AND invw2 GT 0 THEN BEGIN
      yw1[a] = y[invw1]
      yw2[a] = y[invw2]
   ENDIF
ENDFOR
w1 = (A1vsA3+relerr*(A1vsA3+1))/(1-relerr*(A1vsA3+1))
w2 = (A1vsA3-relerr*(A1vsA3+1))/(1+relerr*(A1vsA3+1))
deltaW = w1 - w2
RETURN, (delta = yw1 - yw2)
END
```

References

S. Amari and K. Lodders. Pre-solar grains from supernovae and novae. *Proceedings of the International Astronomical Union*, 2(Highlights of Astronomy 14):349–352, 2006.

S. Auer. Private comunication, 2011.

D. Brownlee, P. Tsou, J. Aléon, C. M. O. '. Alexander, T. Araki, S. Bajt, G. A. Baratta, R. Bastien, P. Bland, P. Bleuet, J. Borg, J. P. Bradley, A. Brearley, F. Brenker, S. Brennan, J. C. Bridges, N. D. Browning, J. R. Brucato, E. Bullock, M. J. Burchell, H. Busemann, A. Butterworth, M. Chaussidon, A. Cheuvront, M. Chi, M. J. Cintala, B. C. Clark, S. J. Clemett, G. Cody, L. Colangeli, G. Cooper, P. Cordier, C. Daghlian, Z. Dai, L. D'Hendecourt, Z. Djouadi, G. Dominguez, T. Duxbury, J. P. Dworkin, D. S. Ebel, T. E. Economou, S. Fakra, S. A. J. Fairey, S. Fallon, G. Ferrini, T. Ferroir, H. Fleckenstein, C. Floss, G. Flynn, I. A. Franchi, M. Fries, Z. Gainsforth, J.-P. Gallien, M. Genge, M. K. Gilles, P. Gillet, J. Gilmour, D. P. Glavin, M. Gounelle, M. M. Grady, G. A. Graham, P. G. Grant, S. F. Green, F. Grossemy, L. Grossman, J. N. Grossman, Y. Guan, K. Hagiya, R. Harvey, P. Heck, G. F. Herzog, P. Hoppe, F. Hörz, J. Huth, I. D. Hutcheon, K. Ignatyev, H. Ishii, M. Ito, D. Jacob, C. Jacobsen, S. Jacobsen, S. Jones, D. Joswiak, A. Jurewicz, A. T. Kearsley, L. P. Keller, H. Khodja, A. L. D. Kilcoyne, J. Kissel, A. Krot, F. Langenhorst, A. Lanzirotti, L. Le, L. A. Leshin, J. Leitner, L. Lemelle, H. Leroux, M.-C. Liu, K. Luening, I. Lyon, G. MacPherson, M. A. Marcus, K. Marhas, B. Marty, G. Matrajt, K. McKeegan, A. Meibom, V. Mennella, K. Messenger, S. Messenger, T. Mikouchi, S. Mostefaoui, T. Nakamura, T. Nakano, M. Newville, L. R. Nittler, I. Ohnishi, K. Ohsumi, K. Okudaira, D. A. Papanastassiou, R. Palma, M. E. Palumbo, R. O. Pepin, D. Perkins, M. Perronnet, P. Pianetta, W. Rao, F. J. M. Rietmeijer, F. Robert, D. Rost, A. Rotundi, R. Ryan, S. A. Sandford, C. S. Schwandt, T. H. See, D. Schlutter, J. Sheffield-Parker, A. Simionovici, S. Simon, I. Sitnitsky, C. J. Snead, M. K. Spencer, F. J. Stadermann, A. Steele, T. Stephan, R. Stroud, J. Susini, S. R. Sutton, Y. Suzuki, M. Taheri, S. Taylor, N. Teslich, K. Tomeoka, N. Tomioka, A. Toppani, J. M. Trigo-

Rodríguez, D. Troadec, A. Tsuchiyama, A. J. Tuzzolino, T. Tyliszczak, K. Uesugi, M. Velbel, J. Vellenga, E. Vicenzi, L. Vincze, J. Warren, I. Weber, M. Weisberg, A. J. Westphal, S. Wirick, D. Wooden, B. Wopenka, P. Wozniakiewicz, I. Wright, H. Yabuta, H. Yano, E. D. Young, R. N. Zare, T. Zega, K. Ziegler, L. Zimmerman, E. Zinner, and M. Zolensky. Comet 81P/Wild 2 Under a Microscope. *Science*, 314: 1711–1716, 2006.

J. Canny. A computational approach to edge detection. *IEEE Trans. Pattern Anal. Mach. Intell.*, 8:679–698, November 1986.

COULOMB. Integrated Engineering Software, 2011. URL http://www.integratedsoft.com.

G. Eichhorn. Measurements of the light flash produced by high velocity particle impact. *Planetary and Space Science*, 23(11):1519 – 1525, 1975.

H. Fechtig, E. Grün, and J. Kissel. *Cosmic Dust*. John Wiley and Sons, 1978.

G. J. Flynn, P. Bleuet, J. Borg, J. P. Bradley, F. E. Brenker, S. Brennan, J. Bridges, D. E. Brownlee, E. S. Bullock, M. Burghammer, B. C. Clark, Z. R. Dai, C. P. Daghlian, Z. Djouadi, S. Fakra, T. Ferroir, C. Floss, I. A. Franchi, Z. Gainsforth, J.-P. Gallien, P. Gillet, P. G. Grant, G. A. Graham, S. F. Green, F. Grossemy, P. R. Heck, G. F. Herzog, P. Hoppe, F. Hörz, J. Huth, K. Ignatyev, H. A. Ishii, K. Janssens, D. Joswiak, A. T. Kearsley, H. Khodja, A. Lanzirotti, J. Leitner, L. Lemelle, H. Leroux, K. Luening, G. J. MacPherson, K. K. Marhas, M. A. Marcus, G. Matrajt, T. Nakamura, K. Nakamura-Messenger, T. Nakano, M. Newville, D. A. Papanastassiou, P. Pianetta, W. Rao, C. Riekel, F. J. M. Rietmeijer, D. Rost, C. S. Schwandt, T. H. See, J. Sheffield-Parker, A. Simionovici, I. Sitnitsky, C. J. Snead, F. J. Stadermann, T. Stephan, R. M. Stroud, J. Susini, Y. Suzuki, S. R. Sutton, S. Taylor, N. Teslich, D. Troadec, P. Tsou, A. Tsuchiyama, K. Uesugi, B. Vekemans, E. P. Vicenzi, L. Vincze, A. J. Westphal, P. Wozniakiewicz, E. Zinner, and M. E. Zolensky. Elemental Compositions of Comet 81P/Wild 2 Samples Collected by Stardust. *Science*, 314:1731–1735, December 2006.

J.P. Freidberg. *Plasma physics and fusion energy*. Cambridge University Press, 2007.

J. Friichtenicht. Experiments on the impact-light-flash at high velocities. Technical Report N66-21095, National Aeronautics and Space Administration - Washington, D. C., 1966.

E. Grün and M. Landgraf. Fast dust in the heliosphere. *Space Science Reviews*, 99: 151–164, 2001.

E. Grün, H. A. Zook, M. Baguhl, A. Balogh, S. J. Bame, H. Fechtig, R. Forsyth, M. S. Hanner, M. Horanyi, J. Kissel, B.-A. Lindblad, D. Linkert, G. Linkert, I. Mann, J. A. M. McDonnell, G. E. Morfill, J. L. Phillips, C. Polanskey, G. Schwehm, N. Siddique, P. Staubach, J. Svestka, and A. Taylor. Discovery of Jovian dust streams and interstellar grains by the ULYSSES spacecraft. *Nature*, 362:428–430, April 1993.

E. Grün, B. Gustafson, I. Mann, M. Baguhl, G. E. Morfill, P. Staubach, A. Taylor, and H. A. Zook. Interstellar dust in the heliosphere. *Astronomy and Astrophysics*, 286:915–924, June 1994.

E. Grün, B. Gustafson, S. Dermot, and H. Fechting. *Interplanetary Dust*. Springer, Berlin, Heidelberg, 2001.

J. K. Hillier, S. Sestak, S. F. Green, F. Postberg, R. Srama, and M. Trieloff. The production of platinum-coated silicate nanoparticle aggregates for use in hypervelocity impact experiments. *Planetary and Space Science*, 57(14-15):2081 – 2086, 2009.

K. Hornung, Yu.G. Malama, and K. Thoma. Modeling of the very high velocity impact process with respect to in-situ ionization measurements. *Advances in Space Research*, 17(12):77 – 86, 1996.

A. Mocker. Optimierung der Strahlfokussierung am Heidelberger Staubbeschleuniger. Master's thesis, Universität Heidelberg, 2002.

A. Mocker. *Comparison of impact ionisation plasma with laser ablation*. PhD thesis, Universität Heidelberg, 2011.

W. Nolting. *Grundkurs Theoretische Physik, 3 Electrodynamik*. Vieweg, Berlin, 1997.

C. C. Porco, P. Helfenstein, P. C. Thomas, A. P. Ingersoll, J. Wisdom, R. West, G. Neukum, T. Denk, R. Wagner, T. Roatsch, S. Kieffer, E. Turtle, A. McEwen, T. V. Johnson, J. Rathbun, J. Veverka, D. Wilson, J. Perry, J. Spitale, A. Brahic, J. A. Burns, A. D. Del Genio, L. Dones, C. D. Murray, and S. Squyres. Cassini Observes the Active South Pole of Enceladus. *Science*, 311:1393–1401, March 2006.

R. Srama. Enhancements and applications of dust accelerator. Technical Report TN1-MPIK-RS-18674-2005001, Max Planck Institute for Nuclear Physics - Heidelberg, 2005.

R. Srama and S. Auer. Low-charge detector for the monitoring of hyper-velocity micron-sized dust particles. *Measurement Science and Technology*, 19(5):055203, 2008.

M. Stübig, G. Schäfer, T. M. Ho, R. Srama, and E. Grün. Laboratory simulation improvements for hypervelocity micrometeorite impacts with a new dust particle source. *Planetary and Space Science*, 49(8, Sp. Iss. SI):853–858, JUL 2001.

A. A. Sysoev, V. P. Ivanov, T. V. Barinova (Komova), Yu. A. Surkov, and V. V. Vysochkin. Mass spectra formation from charged microparticles. *Nuclear Instruments and Methods in Physics Research Section B: Beam Interactions with Materials and Atoms*, 122(1):79 – 83, 1997.

D. F. A. Winters, M. Vogel, D. M. Segal, and R. C. Thompson. Electronic detection of charged particle effects in a Penning trap. *JOURNAL OF PHYSICS B - ATOMIC MOLECULAR AND OPTICAL PHYSICS*, 39(14):3131–3143, JUL 28 2006.

Acknowledgements

I offer my regards and blessings to all of those who supported me in any respect during the completion of this thesis.

I am grateful to my supervisors Dr. Ralf Srama and Prof. Dr. Eberhard Grün, whose encouragement, advice and assistance enabled me to develop an understanding of the thesis topic. Through their commitment I developed a particular interest in the field. I would also like to thank them for their support and help in planning my future career.

I wish to thank those who helped me with the experiments and data evaluation of my thesis. Sebastian Bugiel supported me patiently during the experiments and their set up. He taught me a lot of useful accelerator knowledge and working with him in the laboratory has always been a good time. Dr. Anna Mocker was always available for questions and advice. She helped me to over come many difficulties during the experiments, the data evaluation, and thesis writing. Dr. Sascha Kempf assisted me in writing the evaluation code and taught me valuable knowledge of programming.

I want to express my special gratitude to Dr. Zoltan Sternovsky and Jianfeng Xie from the Laboratory for Atmospheric and Space Physics at the University of Colorado at Boulder. They provided accurate COULOMB simulation and an extensive assistance with the interpretation of the calculated data. I would like to especially thank them for their patience with my numerous emails and requests.

I would like to show my gratitude to Günther Matt, Günther Baust and their trainee Andrej Winter for developing and preparing the calibration set up. With great commitment they helped me to understand the functionality and electronics of the detector and its components. They took time to teach me to solder and were always available for various questions.

I would like to thank Dr. Siegfried Auer for his effort in simulating the detector assembly and for his description of the charge amplifiers.

I am indebted to the Cosmic Dust Group in Heidelberg for providing a stimulating and friendly environment to write a thesis.

I would like to thank Dr. Jonathan Hillier for proofreading this thesis.

Lastly, I wish to thank my family and especially my Oma Lilo for supporting me during my studies that made this thesis possible. They always believed in my competence and success.

Erklärung:

Ich versichere, dass ich diese Arbeit selbstsändig verfasst habe und keine anderen als die angegebenen Quellen und Hilfsmittel benutzt habe.

Heidelberg, den 13. Juli 2011 .....